Supporting Information

Comparative Study of Metal-Organic Frameworks Synthesized via Imide Condensation and Coordination Assembly

Qiao Liu, Jordon S. Hilliard, Zhongzheng Cai, and Casey R. Wade*

Department of Chemistry and Biochemistry, The Ohio State University, Columbus, OH 43210, United States

* E-mail: wade.521@osu.edu

Table of Contents:

Table S1. Summary of MCOFs synthesized by connecting metal organic clusters.

MCOF	Metal Organic Cluster	Linkage type	BET Surface area (m^2/g)	Reference
1-PMDI (This work)	$Zn_5(bt\text{-}NH_2)_3Cl_4$	Imide	30	-
1-NDI (This work)	$Zn_5(bt\text{-}NH_2)_3Cl_4$		408	-
1-BPDI (This work)	$Zn_5(bt\text{-}NH_2)_3Cl_4$		447	-
1-HFIPI (This work)	$Zn_5(bt\text{-}NH_2)_3Cl_4$		483	-
JNM-1	$Cu(I)_3(PyCA)_3$ [a]	Imine	535	1
JNM-2	$Cu(I)_3(PyCA)_3$ [a]		505	1
FDM-71	$Cu(I)_3(PyCA)_3$ [a]		1135	2
JNM-3-AA	$Cu(I)_3(PyCA)_3$ [a]		696	3
Ti-COF-1	$Na_2Ti(2,3\text{-}DHTA)_3$ [b]		1000	4
MOF-901	$[Ti_6O_6(OiPr)_6(AB)_6]$ [c]		550	5
CCF-1-SE	$[Cr_3(\mu_3\text{-}O)(RCO_2)_6]NO_3$ [d]		301	6
Ni-Py-COF	$Ni(dbpag)_2$ [e]		1051	7
Ni-Bn-COF	$Ni(dbpag)_2$ [e]		1240	7
RuCOF-ETTA	$Ru(bpy)_3^{2+}$ [f]		124	8
RuCOF-TPB	$Ru(bpy)_3^{2+}$ [f]		149	8
RuCOF-ETTBA	$Ru(bpy)_3^{2+}$ [f]		235	8
$[Zn_4(dipp)_4(L_1)_2]_n$	$[Zn(dipp)(4\text{-}Py\text{-}CHO)]_4$ [g]		124	9

[a] PyCA = pyrazolate-4-carboxaldehyde
[b] 2,3-DHTA = 2,3-dihydroxyterephthalaldehyde
[c] AB = 4-aminobenzoate; OiPr = isopropoxide
[d] R = 4-aminophenyl
[e] Hdbpag = 1,2-bis(4'-amino-[1,1'-biphenyl]-4-yl)ethane-1,2-dione
[f] bpy = bipyridine
[g] dipp = diiminopyridine

Table S2. Comparison of surface area between reported porous polyimides and **1-XDI** MOFs.

Porous polyimides	Surface area (m^2/g)	Reference
sPI-A-H	25	10
sPI-M-H	492	
sPI-A-B	620	
sPI-M-B	618	
NPI-1	721	11
NPI-2	291	
NPI-3	373	
MPI-1	1454	12
MPI-2	814	
MPI-3	586	
PPI-1	18	13
PPI-2	604	
PPI-3	717	
PI1	660	14
PI2	265	
PI3	366	
1-PMDI	30	**This work**
1-NDI	408	
1-BPDI	447	
1-HFIPI	483	

Part 1: Characterization data for 1-NH_2 and 1-XDI MOFs

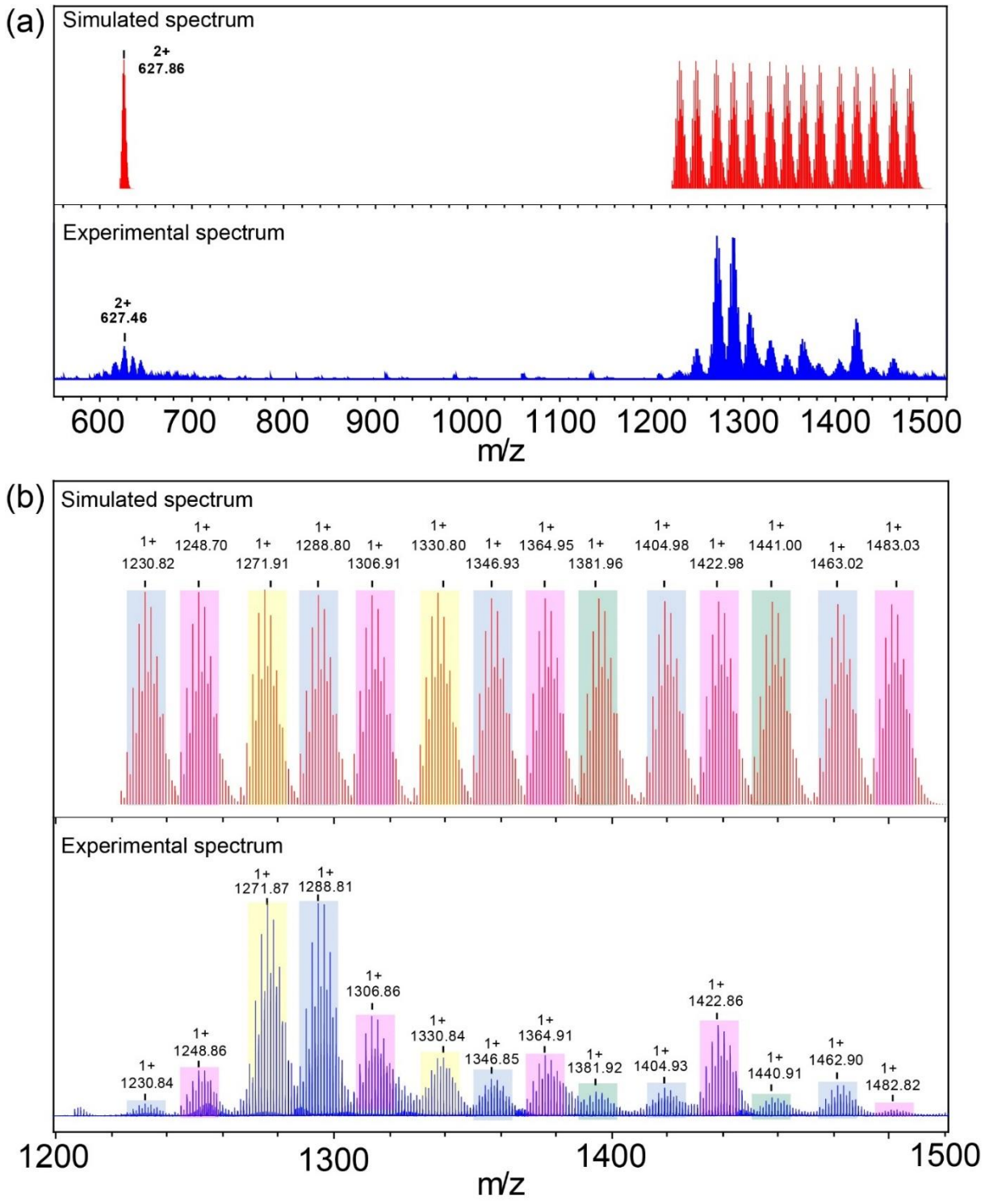

Figure S1. Simulated and experimental ESI-MS spectrum of **1-NH_2**

Sample dissolved in acetone and measured in positive mode with m/z range from 550-1520 (a) and 1200-1500 (b).

Table S3. Assignment of ions observed in the ESI-MS spectrum shown in Figure S1.

Assignments	Highlight color	m/z Experimental	m/z Simulated
$Zn_5Cl_3(C_6H_5N_4)_6^+$	Blue	1230.84	1230.82
$Zn_5Cl_3(C_6H_5N_4)_6^+ + C_3H_6O$		1288.81	1288.80
$Zn_5Cl_3(C_6H_5N_4)_6^+ + (C_3H_6O)_2$		1346.85	1346.93
$Zn_5Cl_3(C_6H_5N_4)_6^+ + (C_3H_6O)_3$		1404.93	1404.98
$Zn_5Cl_3(C_6H_5N_4)_6^+ + (C_3H_6O)_4$		1462.90	1463.02
$Zn_5Cl_3(C_6H_5N_4)_6^+ + H_2O$	Pink	1248.86	1248.70
$Zn_5Cl_3(C_6H_5N_4)_6^+ + H_2O + C_3H_6O$		1306.86	1306.91
$Zn_5Cl_3(C_6H_5N_4)_6^+ + H_2O + (C_3H_6O)_2$		1364.91	1346.93
$Zn_5Cl_3(C_6H_5N_4)_6^+ + H_2O + (C_3H_6O)_3$		1422.86	1422.98
$Zn_5Cl_3(C_6H_5N_4)_6^+ + H_2O + (C_3H_6O)_4$		1482.82	1483.03
$Zn_5Cl_2(C_6H_5N_4)_6^{2+} + OH^- + C_3H_6O$	Yellow	1271.87	1271.91
$Zn_5Cl_2(C_6H_5N_4)_6^{2+} + OH^- + (C_3H_6O)_2$		1330.83	1330.80
$Zn_5Cl_3(C_6H_5N_4)_6^+ + (H_2O)_2 + (C_3H_6O)_2$	Green	1381.92	1381.96
$Zn_5Cl_3(C_6H_5N_4)_6^+ + (H_2O)_2 + (C_3H_6O)_4$		1440.91	1441.00
$Zn_5Cl_2(C_6H_5N_4)_6^{2+} + (C_3H_6O)$	-	627.46	627.86

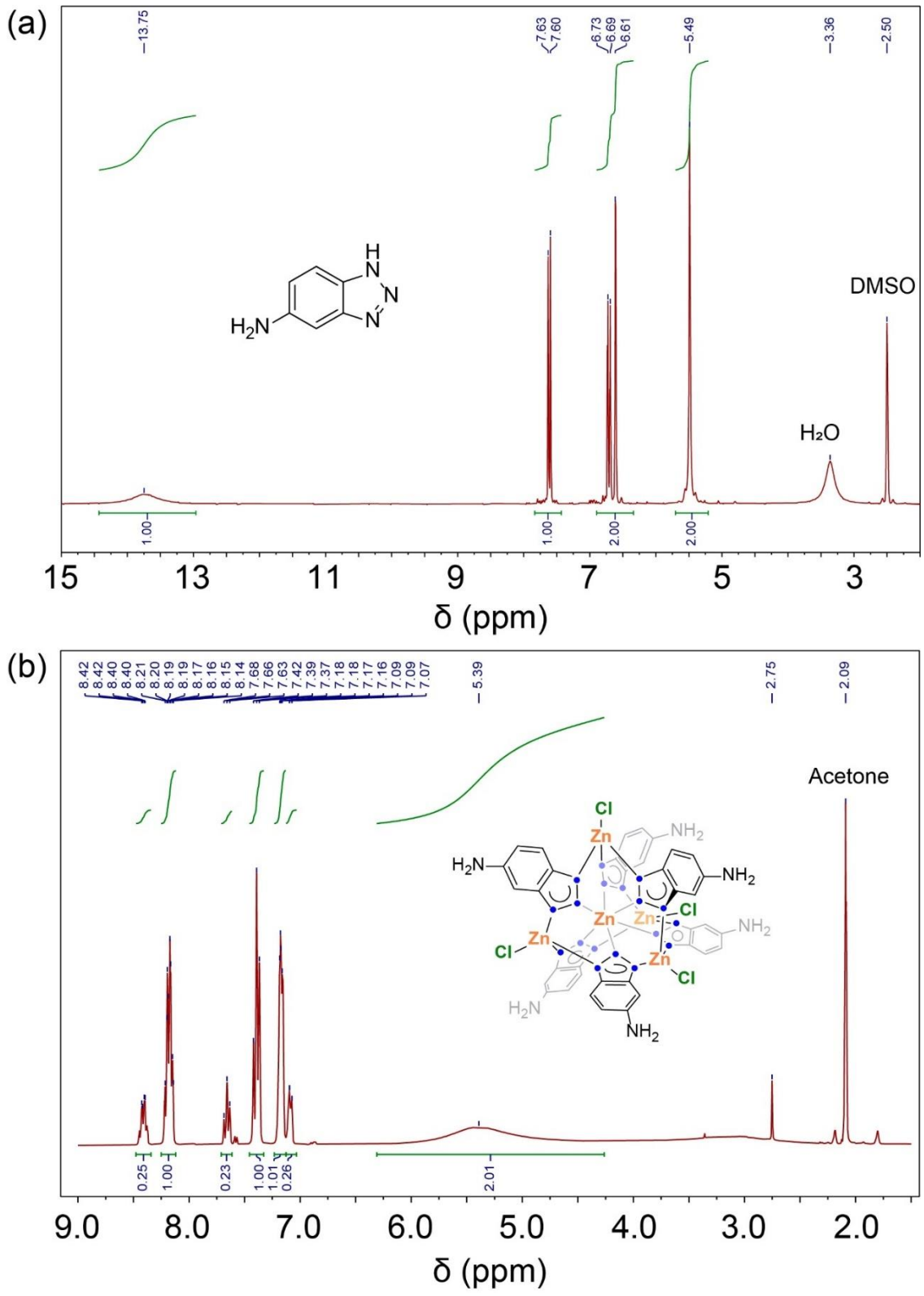

Figure S2. ^{1}H NMR spectra of (a) Hbt-NH_2 and (b) **1-NH_2**.

Spectra measured in acetone-d_6.

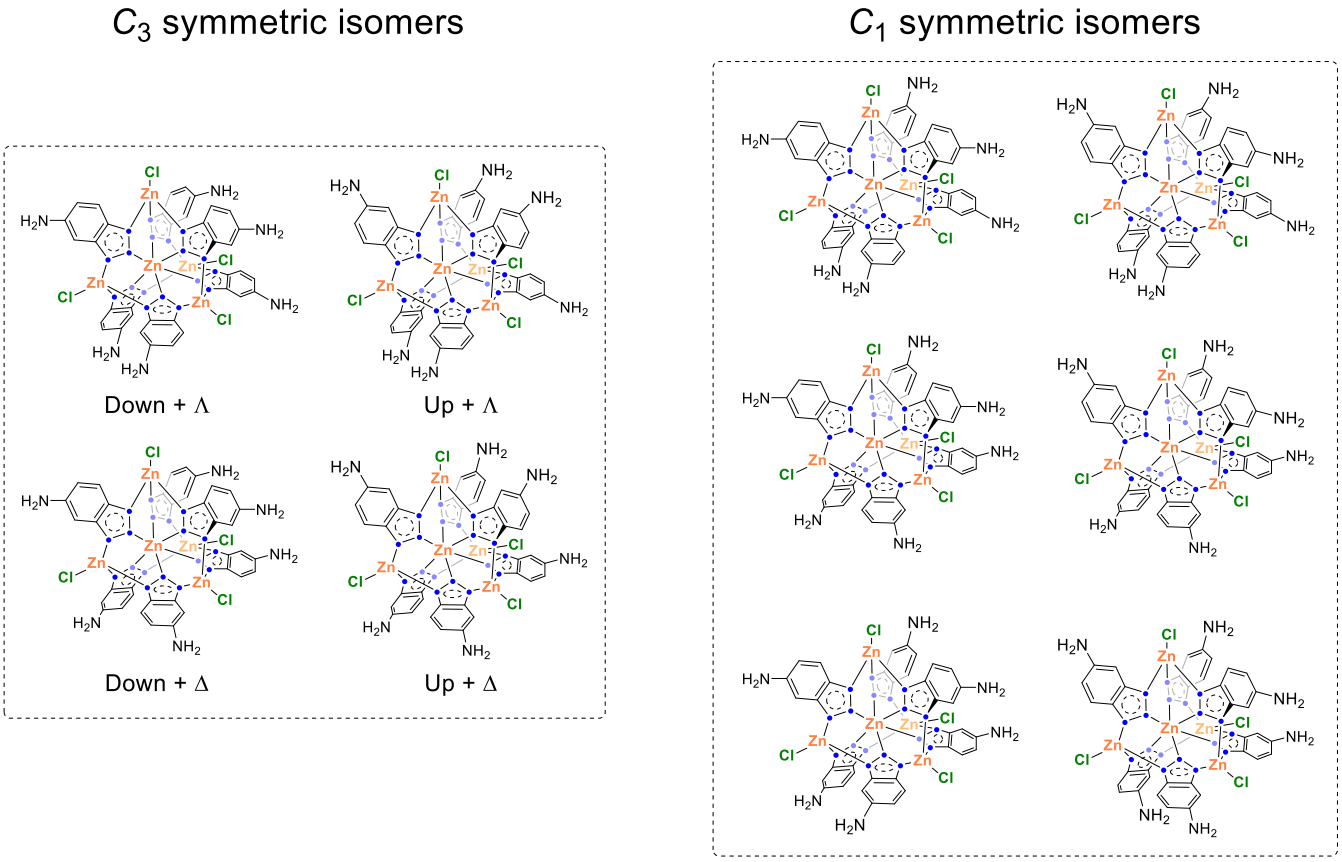

Figure S3. Some possible isomers of **1-NH$_2$**.

C$_3$ and *C*$_1$ symmetric isomers are included on the left and right boxes, respectively.

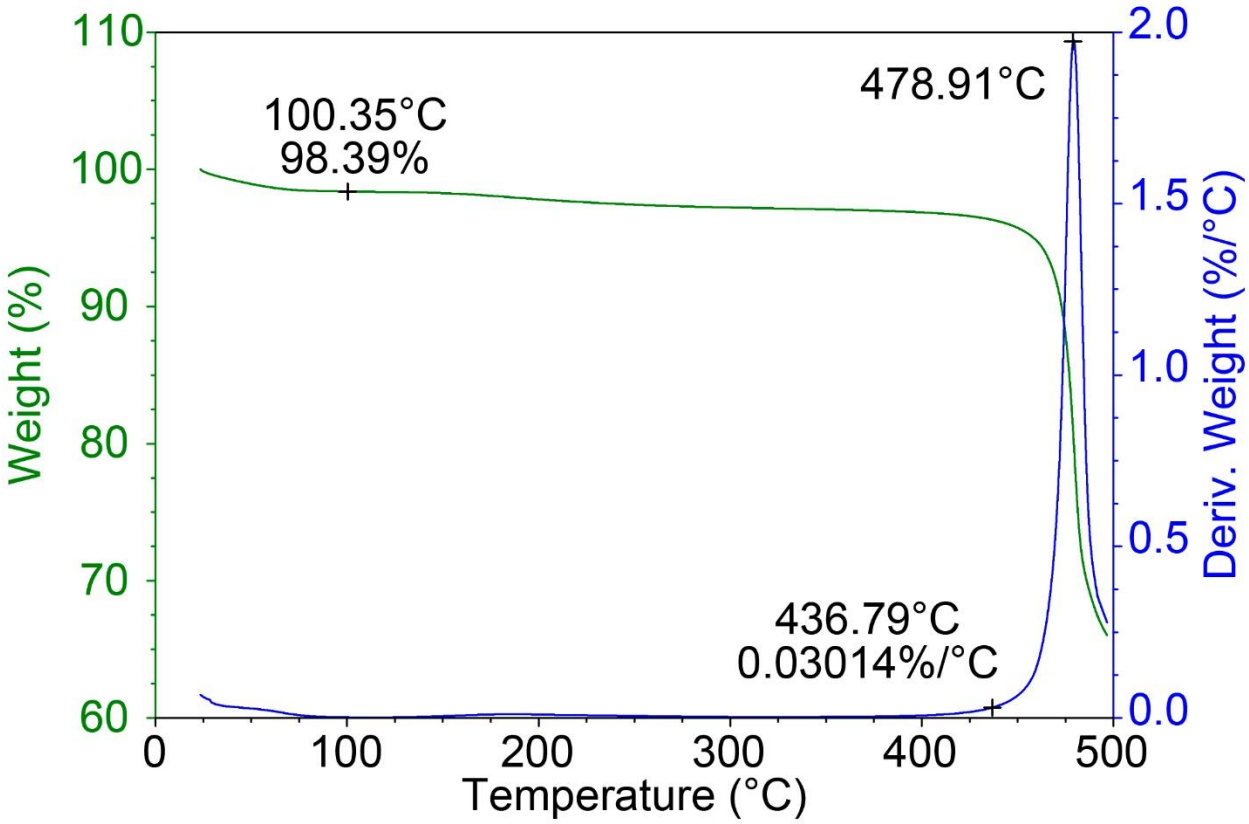

Figure S4. Thermogravimetric analysis data for dried **1-NH_2**.

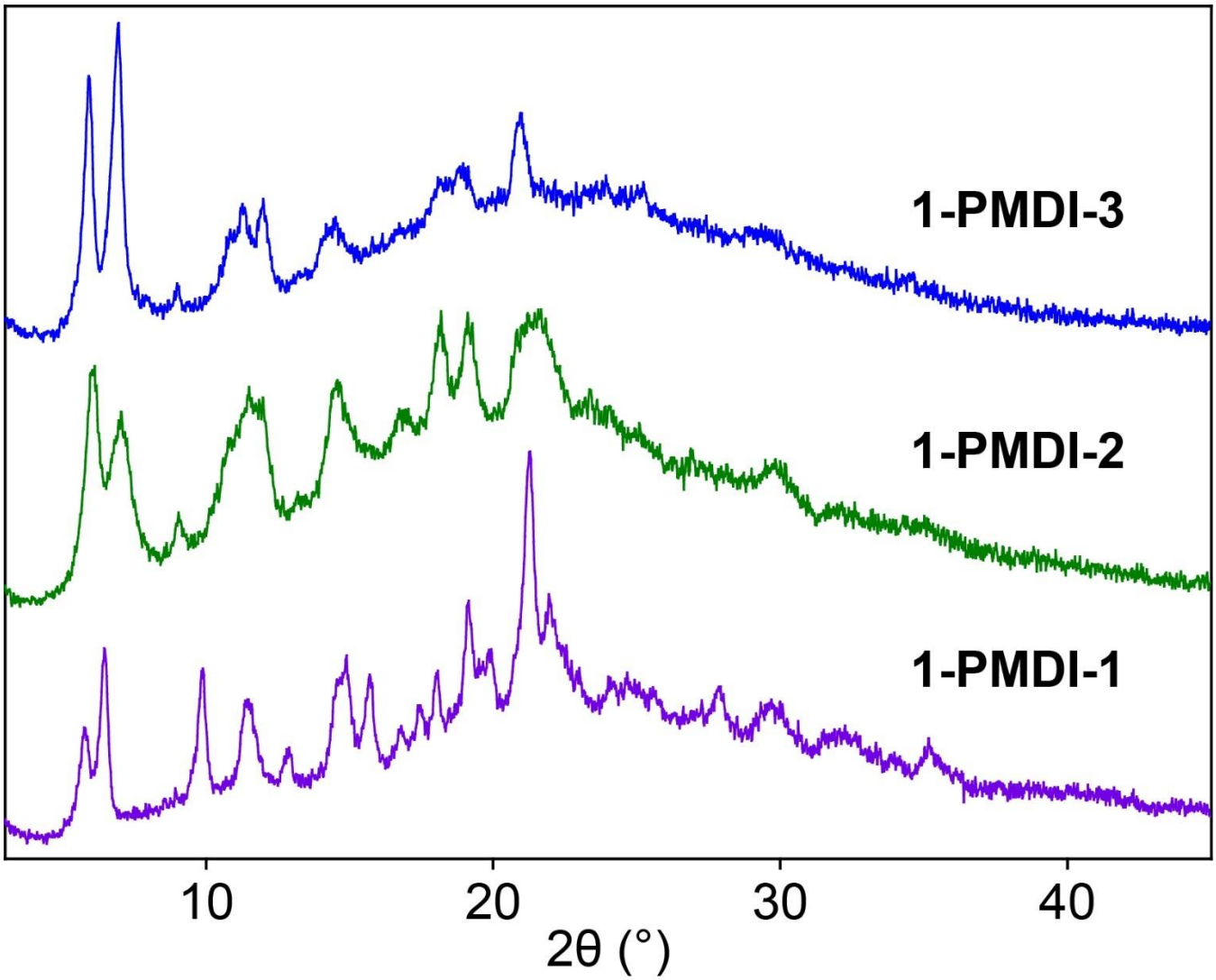

Figure S5. PXRD patterns measured for multiple batches of **1-PMDI**.

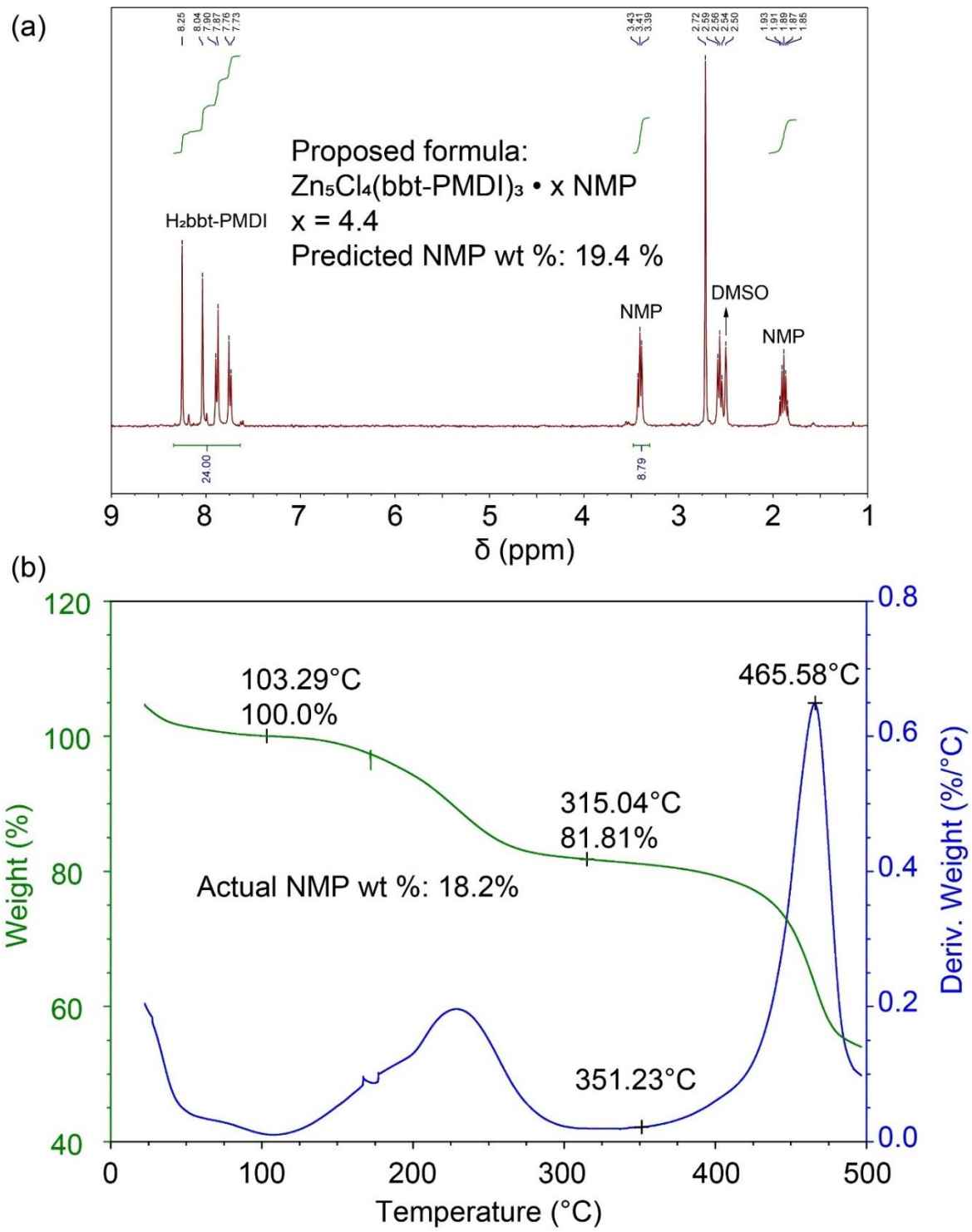

Figure S6. Acid-digested ^{1}H NMR spectrum and TGA data for as-synthesized **1-PMDI**.

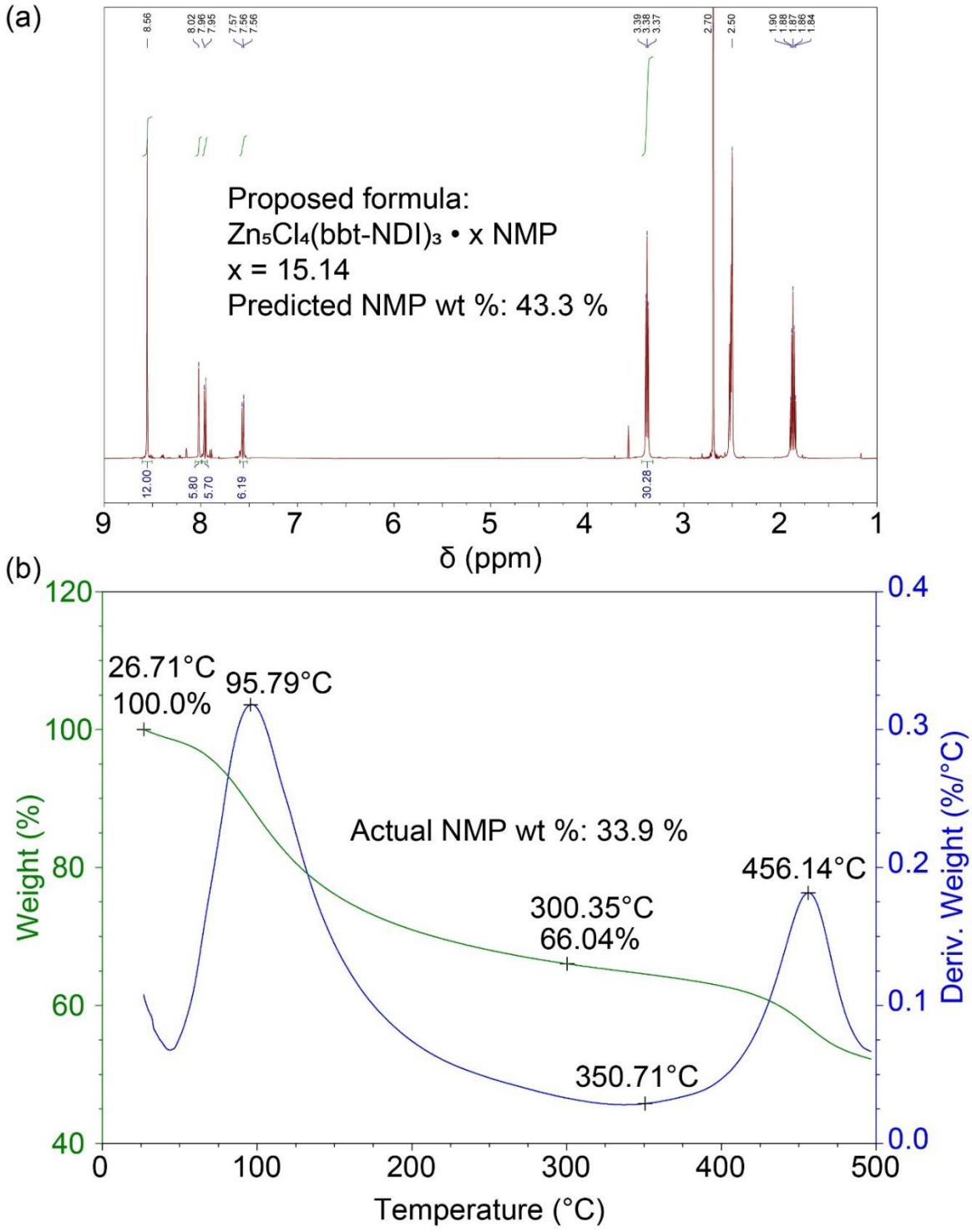

Figure S7. Acid-digested ^{1}H NMR spectrum and TGA data for as-synthesized **1-NDI**.

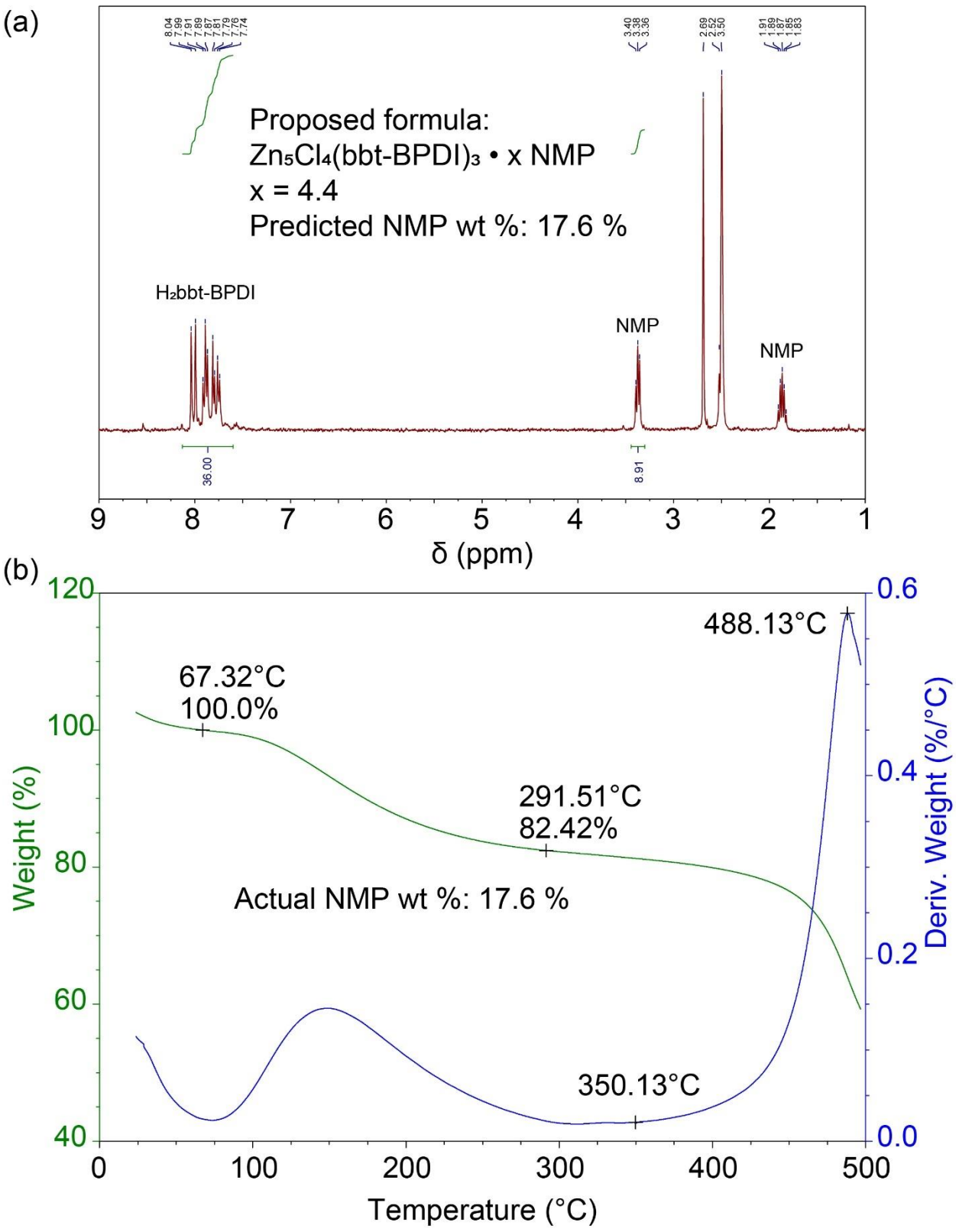

Figure S8. Acid-digested ^{1}H NMR spectrum and TGA data for as-synthesized **1-BPDI**.

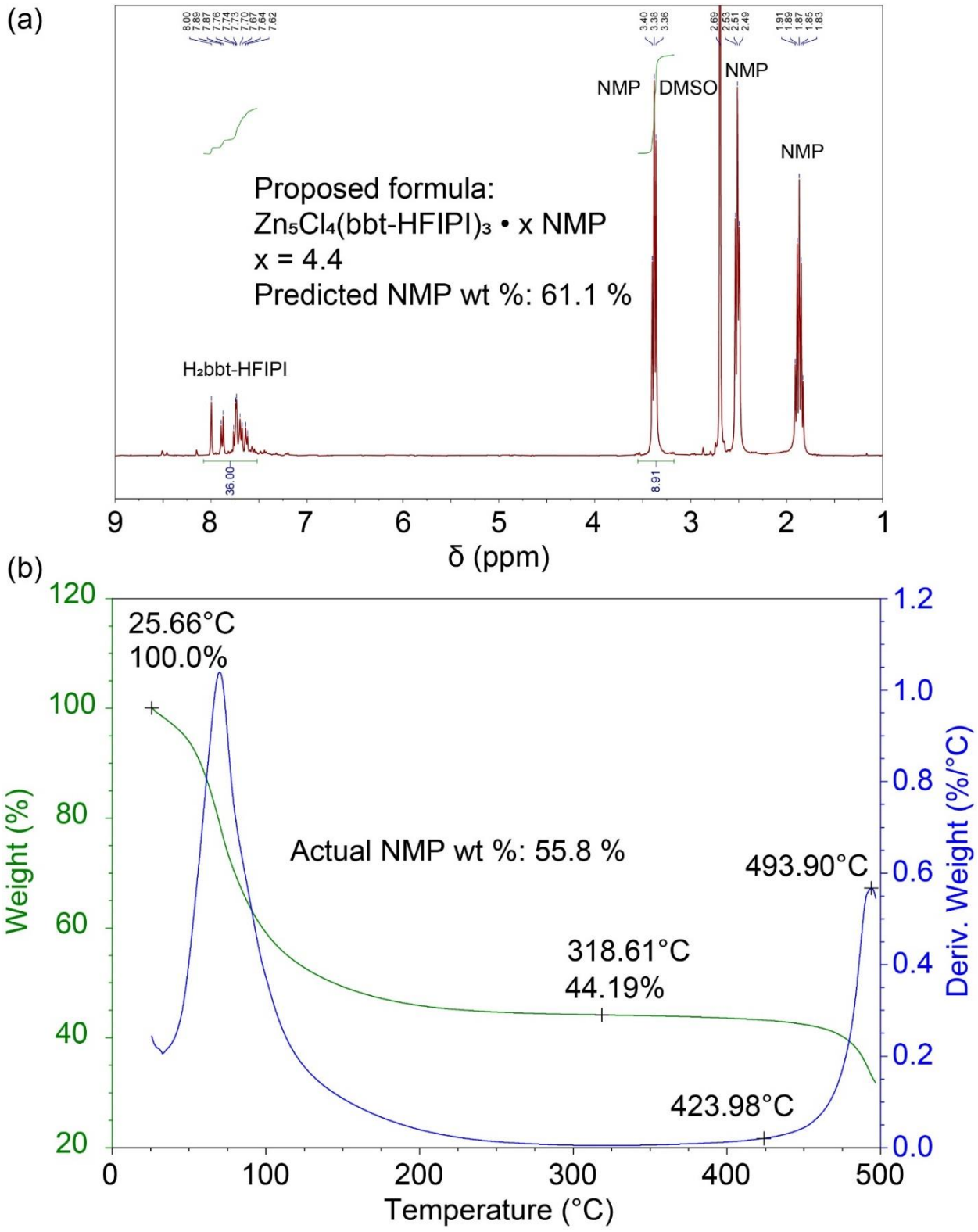

Figure S9. Acid-digested ^{1}H NMR spectrum and TGA data for as-synthesized **1-HFIPI**.

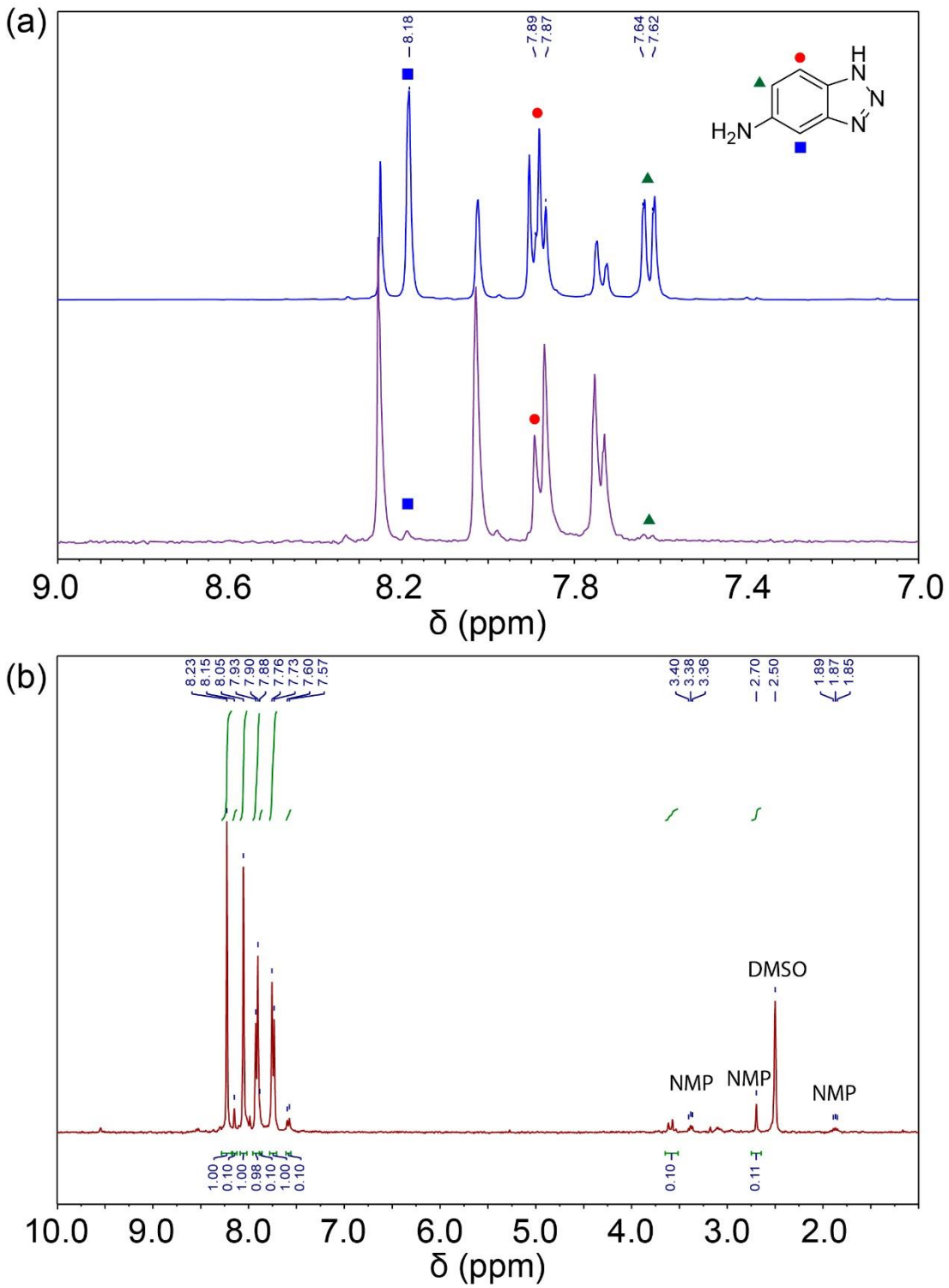

Figure S10. Acid-digested ^{1}H NMR spectrum of activated **1-PMDI.**
(a) Aromatic region of the acid-digested ^{1}H NMR spectra of activated **1-PMDI** (bottom) and the same sample spiked with **Hbt-NH$_2$** to confirm the identity of the unreacted species (top).
(b) Full acid-digested ^{1}H NMR spectrum of activated **1-PMDI**.

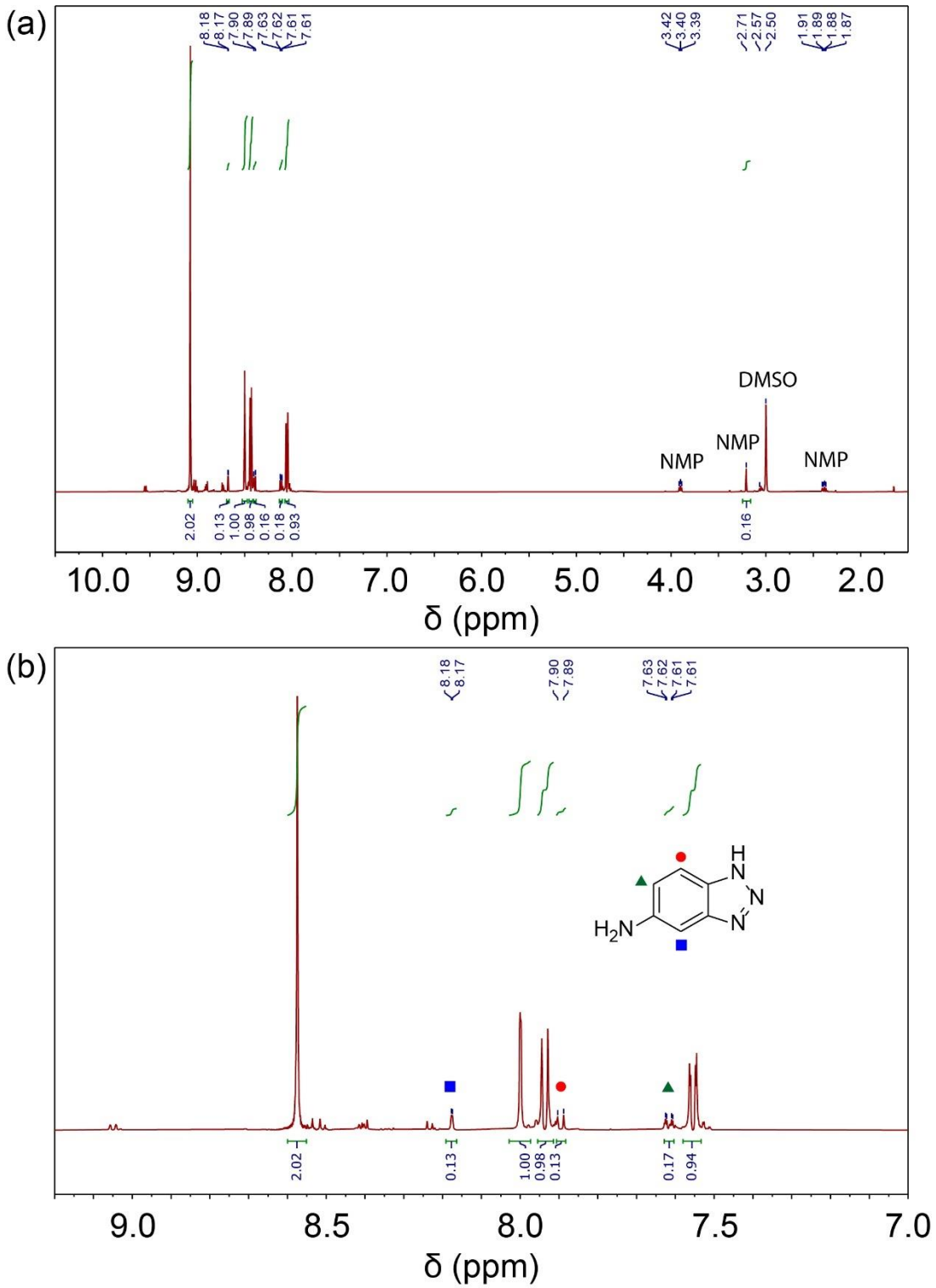

Figure S11. Acid-digested ^{1}H NMR spectrum of activated **1-NDI**.
(a) shows the full spectrum and (b) shows only the aromatic region.

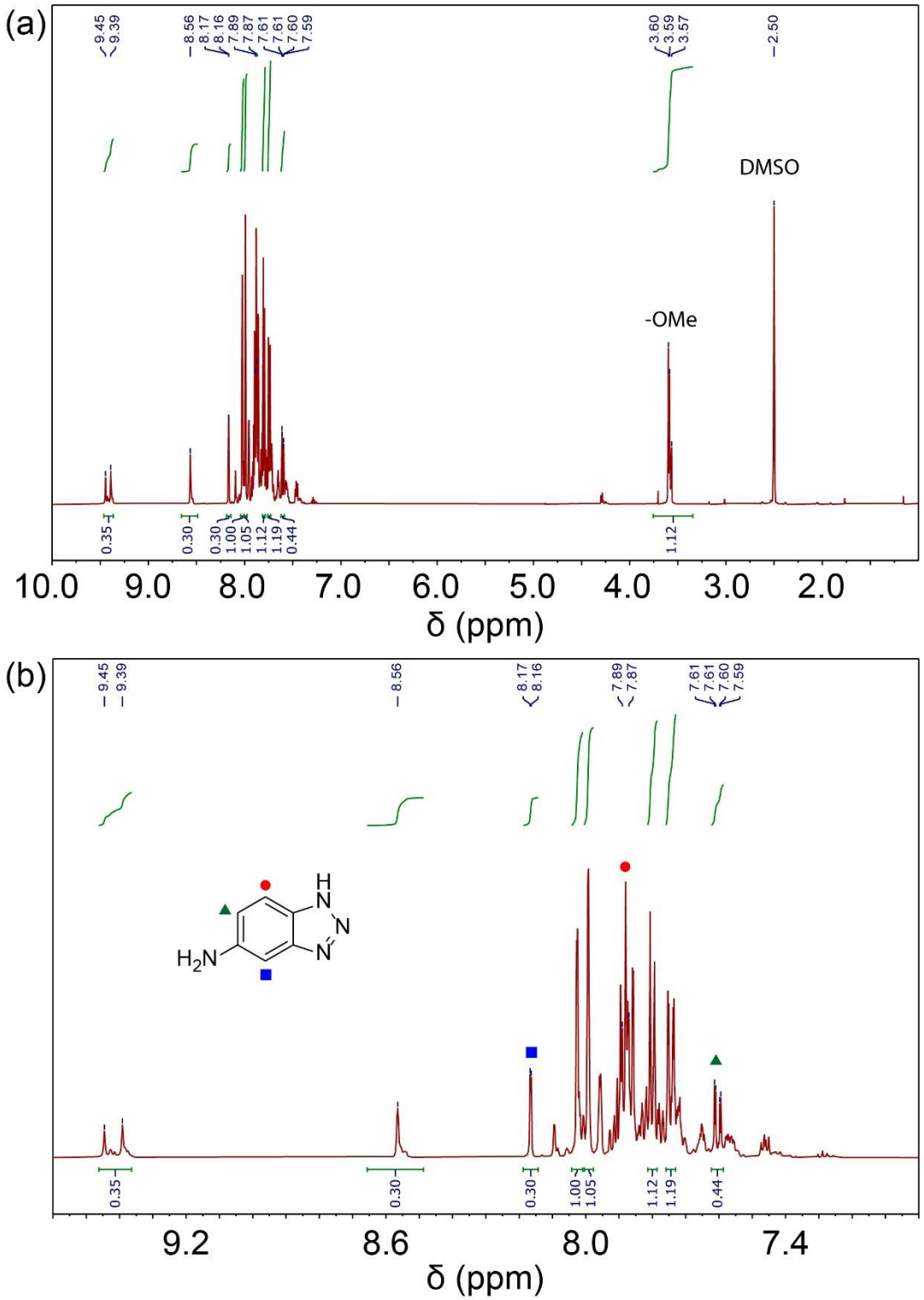

Figure S12. Acid-digested ^{1}H NMR spectrum of activated **1-BPDI**.
(a) shows the full spectrum and (b) shows only the aromatic region.

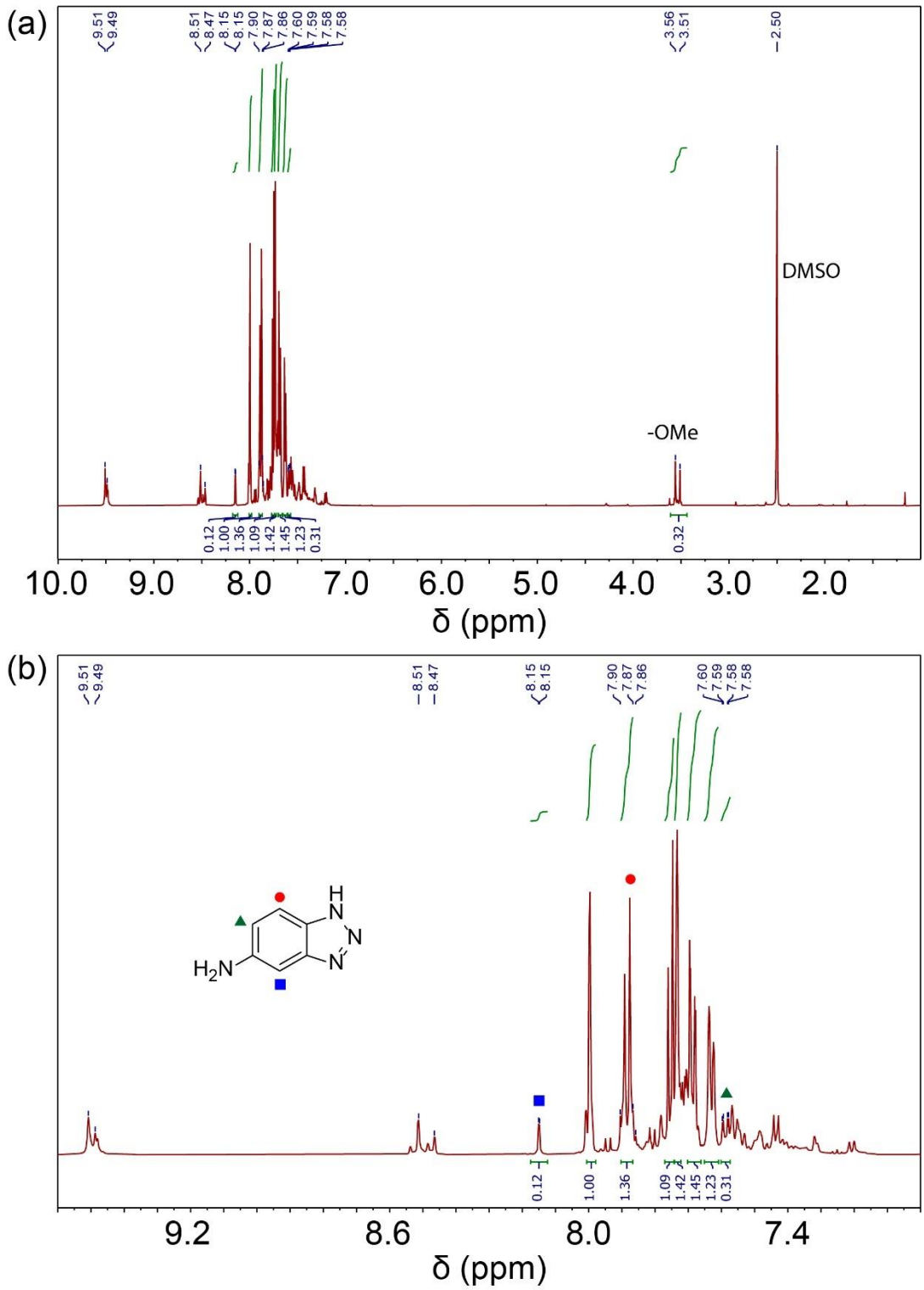

Figure S13. Acid-digested ^{1}H NMR spectrum of activated **1-HFIPI**.
(a) shows the full spectrum and (b) shows only the aromatic region.

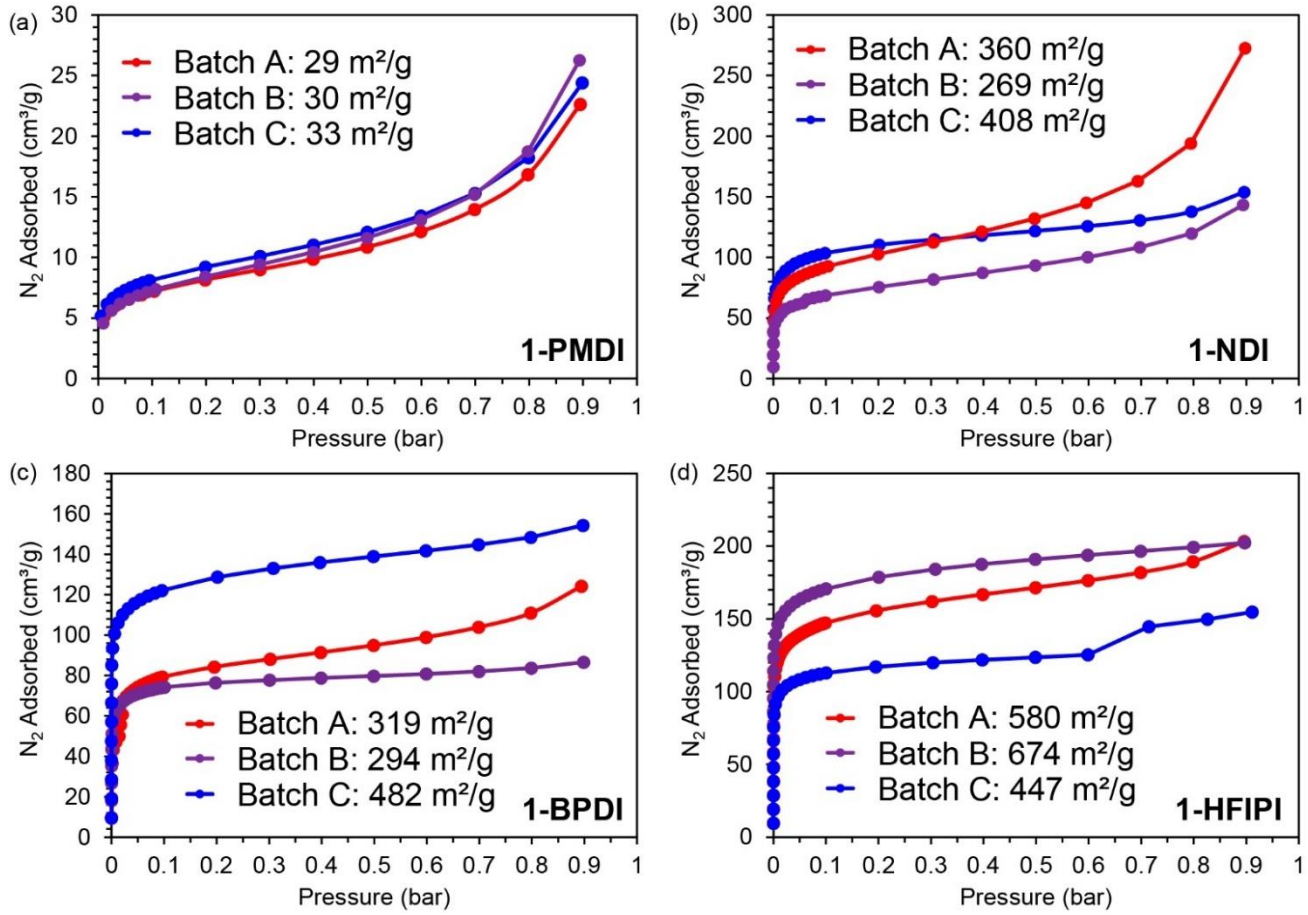

Figure S14. N_2 adsorption isotherms (77 K) and calculated BET surface areas measured for multiple batches of the **1-XDI** MOFs.

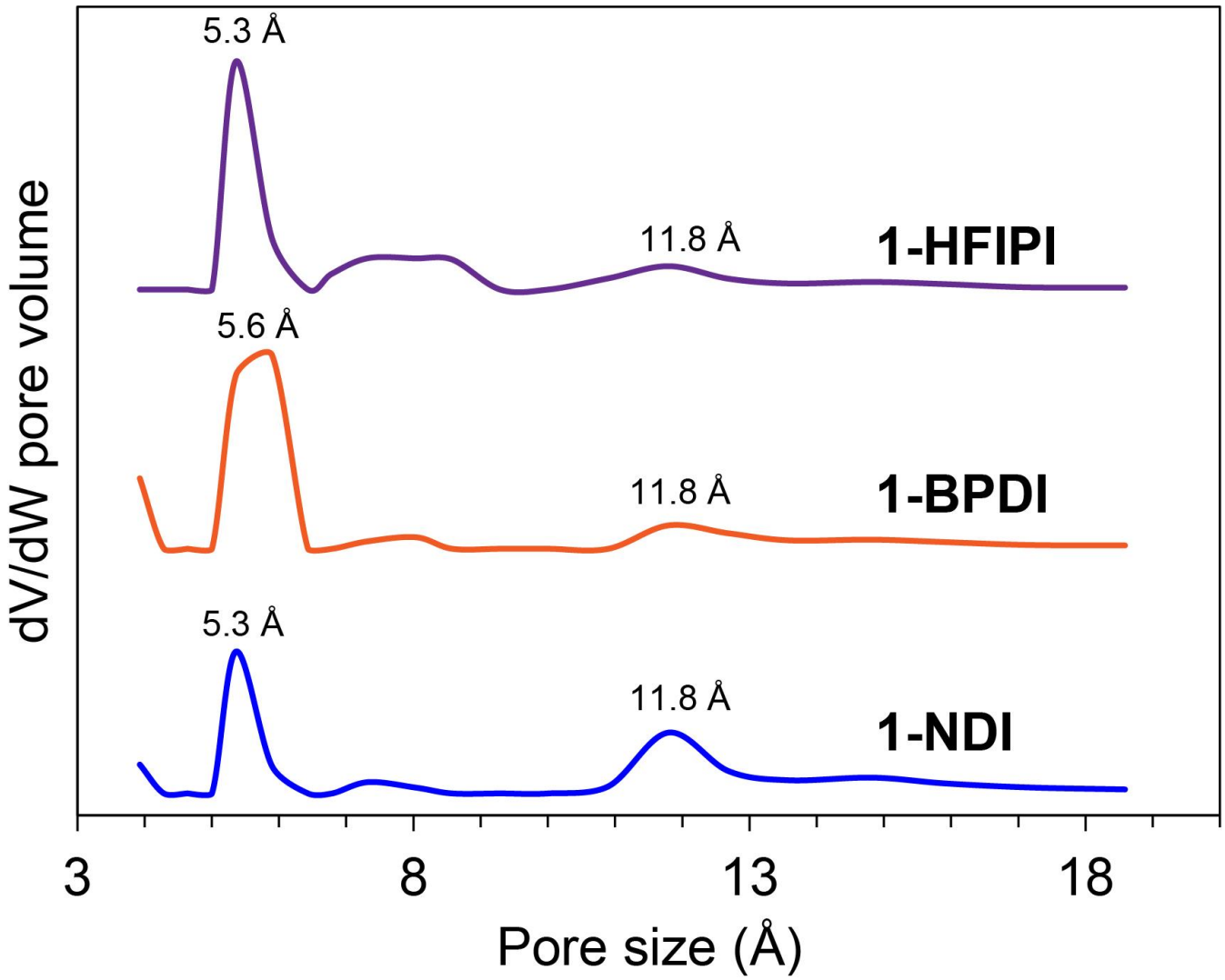

Figure S15. DFT pore size distributions of **1-XDI** MOFs.

DFT pore size distributions have been calculated for the **1-XDI** samples based on the N_2 adsorption isotherm data (Figure S15), except **1-PMDI** due to negligible N_2 uptake. The **1-XDI** samples show the presence of small micropores around 5-6 Å and a smaller volume fraction of micropores with ~12 Å diameter. The presence of relatively small micropores and the similarity in pore size distribution for these materials despite the different linker length indicate that they likely adopt interpenetrated structures.

Elemental analysis and ICP-OES results:

CHN elemental analysis (EA) and ICP-OES analysis of Zn were performed on the **1-XDI 2-XDI** MOFs. Based on literature precedent (see main text), pentanuclear Zn_5 clusters or nonanuclear Zn_9 clusters were considered as possible SBUs. The corresponding empirical formulas have been included with the data in Table S4-Table S11 below. The sum of squares error (SSE) between the theoretical and experimental EA and ICP-OES results have been calculated as a means of comparing the goodness-of-fit of the experimental results with the proposed empirical formulas.

Table S4. Elemental analysis and ICP results for **1-PMDI**.

Elements	Theo. %: Zn_5	Exp. %	Error: Zn_5
C	43.70	45.95	-2.25
H	1.33	1.74	-0.41
N	18.53	19.56	-1.03
Zn	18.02	19.41	-1.39
		SSE:	**8.20**

Zn_5 empirical formula: $Zn_5Cl_4(bbt\text{-}PMDI)_3$, $C_{66}H_{24}Cl_4N_{24}O_{12}Zn_5$

Table S5. Elemental analysis and ICP results for **1-BPDI**.

Elements	Theo. %: Zn_5	Exp. %	Error: Zn_5
C	49.40	50.51	-1.11
H	1.78	2.21	-0.43
N	16.46	16.51	-0.05
Zn	16.01	14.01	2.00
		SSE:	**5.42**

Zn_5 empirical formula: $Zn_5Cl_4(bbt\text{-}BPDI)_3$, $C_{84}H_{36}Cl_4N_{24}O_{12}Zn_5$

Table S6. Elemental analysis and ICP results for **1-NDI**.

Elements	Theo. %: Zn_5	Exp. %	Error: Zn_5
C	47.70	48.78	-1.08
H	1.54	2.08	-0.54
N	17.12	17.1	0.02
Zn	16.65	14.28	2.37
		SSE:	**7.07**

Zn_5 empirical formula: $Zn_5Cl_4(bbt\text{-}NDI)_3$, $C_{78}H_{30}Cl_4N_{24}O_{12}Zn_5$

Table S7. Elemental analysis and ICP results for **1-HFIPI**.

Elements	Theo. %: Zn_5	Exp. %	Error: Zn_5
C	44.82	45.88	-1.06
H	1.46	1.66	-0.20
N	13.49	13.25	0.24
Zn	13.12	13.43	-0.31
		SSE:	**1.32**

Zn_5 empirical formula: $Zn_5Cl_4(bbt\text{-}HFIPI)_3$, $C_{93}H_{36}Cl_4F_{18}N_{24}O_{12}Zn_5$

Table S8. Elemental analysis and ICP results for **2-PMDI**.

Elements	Theo. %: Zn_5	Theo. %: Zn_9	Exp. %	Error: Zn_5	Error: Zn_9
C	46.58	47.61	43.16	3.42	4.45
H	1.90	1.83	2.24	-0.34	-0.41
N	17.62	18.51	15.66	1.96	2.85
			SSE:	**15.65**	**28.09**

Zn_5 and Zn_9 empirical formulas:

$Zn_5(CH_3COO)_4(bbt\text{-}PMDI)_3$: $C_{74}H_{36}N_{24}O_{20}Zn_5$

$Zn_9(CH_3COO)_6(bbt\text{-}PMDI)_6$: $C_{144}H_{66}N_{48}O_{36}Zn_9$

The acid-digested ^1H NMR spectrum of **2-PMDI** shows a low acetate:linker ratio (1:1) that is consistent with Zn_9 cluster building units (Figure S30). However, the high SSE values (>15) do not strongly support empirical formulas derived from either Zn_5 or Zn_9 clusters.

Table S9. Elemental analysis and ICP results for **2-BPDI**.

Elements	Theo. %: Zn_5	Theo. %: Zn_9	Exp. %	Error: Zn_5	Error: Zn_9
C	51.72	52.87	48.98	2.74	3.89
H	2.26	2.22	2.72	-0.46	-0.50
N	15.73	16.44	14.95	0.78	1.49
Zn	15.30	14.39	16.40	-1.10	-2.01
			SSE:	**9.54**	**21.64**

Zn_5 and Zn_9 empirical formulas:

$Zn_5(CH_3COO)_4(bbt\text{-}BPDI)_3$: $C_{92}H_{48}N_{24}O_{20}Zn_5$

$Zn_9(CH_3COO)_6(bbt\text{-}BPDI)_6$: $C_{180}H_{90}N_{48}O_{36}Zn_9$

The acid-digested ^{1}H NMR spectrum of **2-BPDI** shows a lower acetate:linker ratio (0.8 : 1) than would be expected for the presence of Zn_5 or Zn_9 clusters (**Figure S31**). The high SSE values also do not strongly support empirical formulas derived from either Zn_5 or Zn_9 clusters.

Table S10. Elemental analysis and ICP results for **2-NDI**.

Elements	Theo. %: Zn_5	Theo. %: Zn_9	Exp. %	Error: Zn_5	Error: Zn_9
C	47.70	49.41	50.08	-2.38	-0.67
H	1.54	1.60	2.19	-0.65	-0.59
N	17.12	17.73	17.77	-0.65	-0.04
Zn	16.65	15.52	13.82	2.83	1.70
			SSE:	**14.51**	**3.69**

Zn_5 and Zn_9 empirical formulas:

Zn_5Cl_4(bbt-NDI)$_3$: $C_{78}H_{30}Cl_4N_{24}O_{12}Zn_5$

Zn_9Cl_6(bbt-NDI)$_6$: $C_{156}H_{60}Cl_6N_{48}O_{24}Zn_9$

The high SSE values (~10) also do not strongly support empirical formulas derived from either Zn_5 or Zn_9 clusters.

Table S11. Elemental analysis and ICP results for **2-HFIPI**.

Elements	Theo. %: Zn_5	Theo. %: Zn_9	Exp. %	Error: Zn_5	Error: Zn_9
C	44.82	46.08	45.4	-0.58	0.68
H	1.46	1.50	1.94	-0.48	-0.44
N	13.49	13.87	13.70	-0.21	0.17
Zn	13.12	12.14	12.98	0.14	-0.84
			SSE:	**0.64**	**1.39**

Zn_5 and Zn_9 empirical formulas:

Zn_5Cl_4(bbt-HFIPI)$_3$: $C_{93}H_{36}Cl_4F_{18}N_{24}O_{12}Zn_5$

Zn_9Cl_6(bbt-HFIPI)$_6$: $C_{186}H_{72}Cl_6F_{36}N_{48}O_{24}Zn_9$

The relatively low SSE values for **2-HFIPI** reflect a good fit with empirical formulas derived from either Zn_5 or Zn_9 clusters. However, the acid-digested ^{1}H NMR and ATR-IR spectra of **2-HFIPI** show a large percentage of hydrolyzed linker species (**Figure S33** and Figure S34), meaning that **2-HFIPI** is unlikely to contain Zn_5 or Zn_9 clusters.

Part 2: ^{1}H NMR and ATR-IR spectra of H_2bbt-XDI linkers

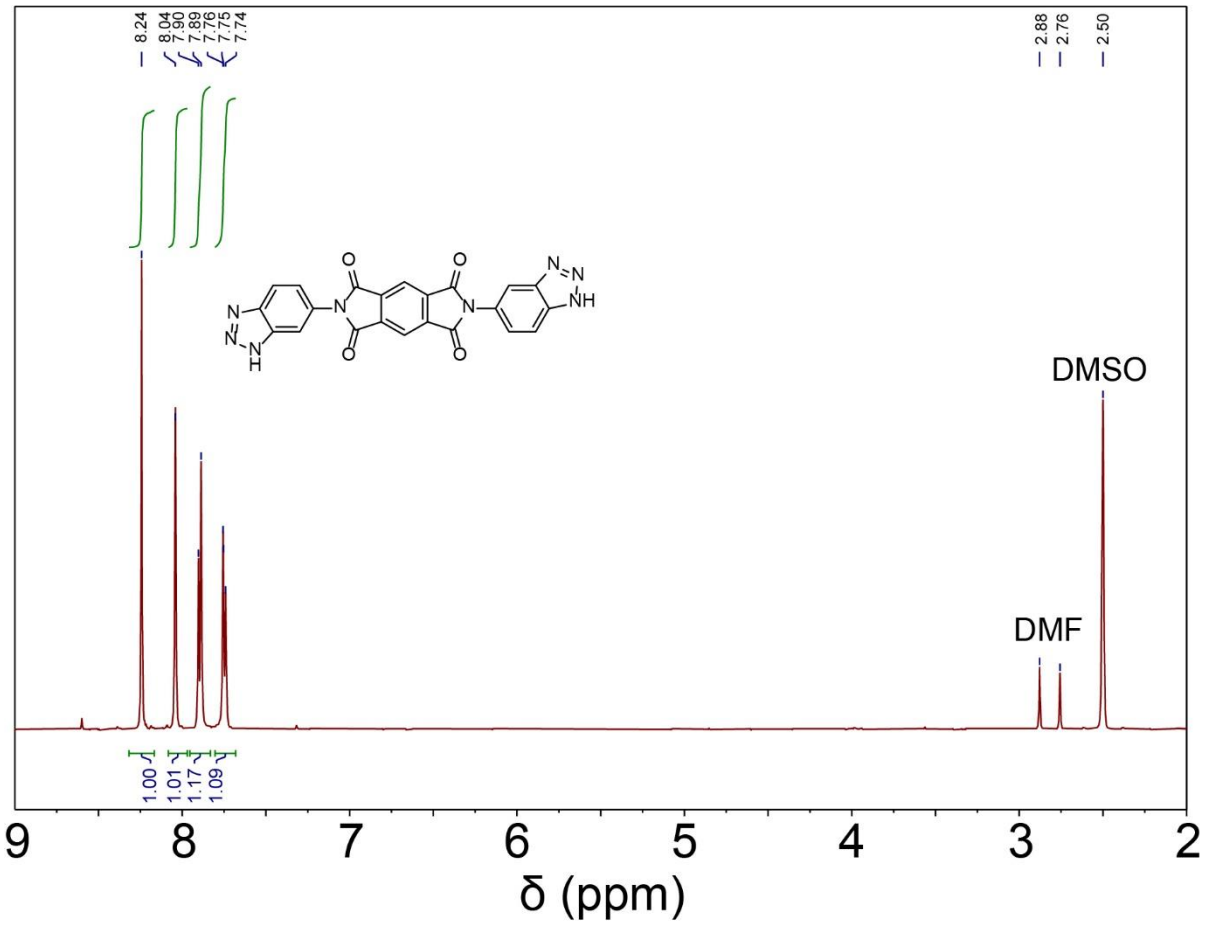

Figure S16. ^{1}H NMR spectrum of H_2bbt-PMDI.
The sample was dissolved in trifluoroacetic acid and sSeveral drops of DMSO-d_6 were added to the solution to provide a lock signal for shimming.

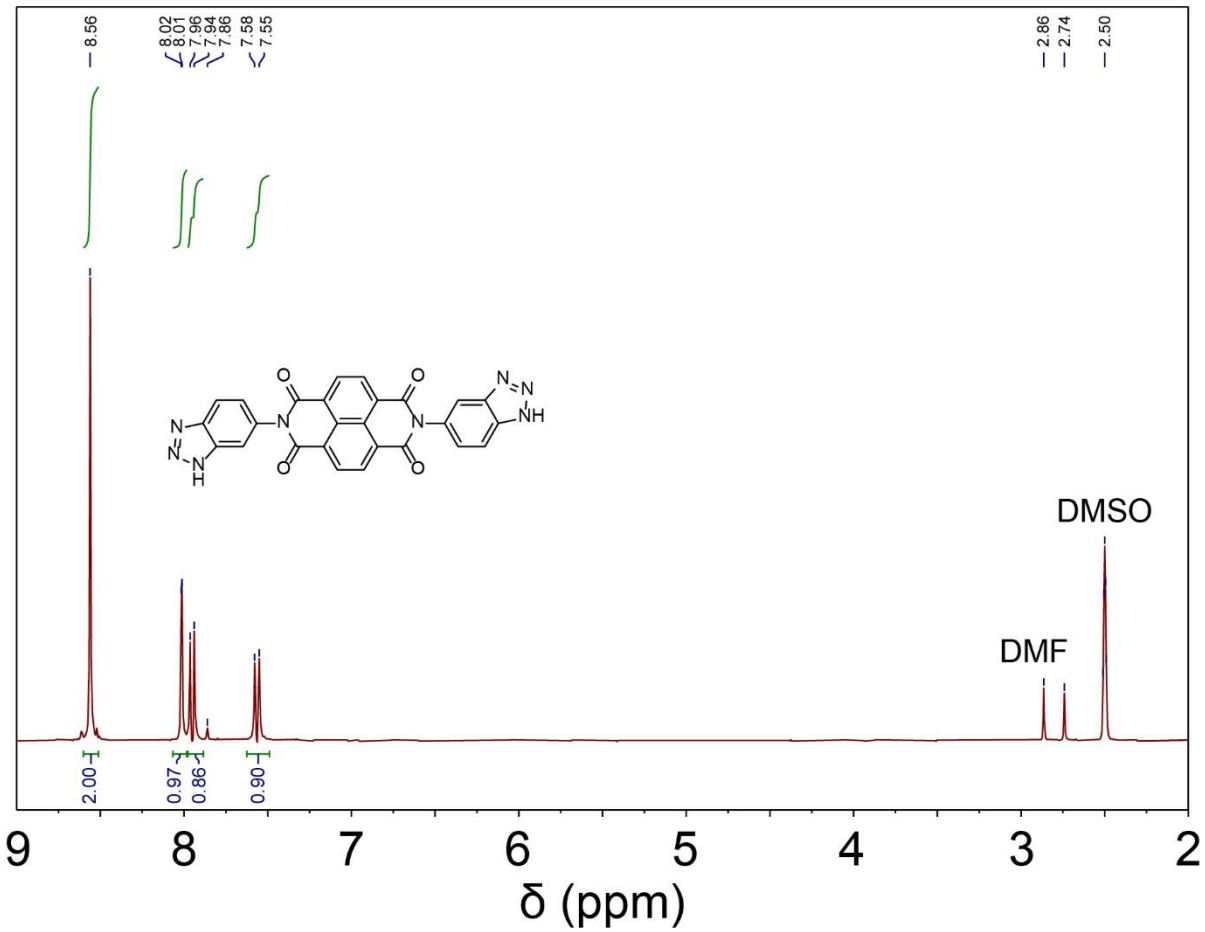

Figure S17. ^{1}H NMR spectrum of H_2bbt-NDI.
The sample was dissolved in trifluoroacetic acid. Several drops of DMSO-d_6 were added to the solution to provide a lock signal for shimming.

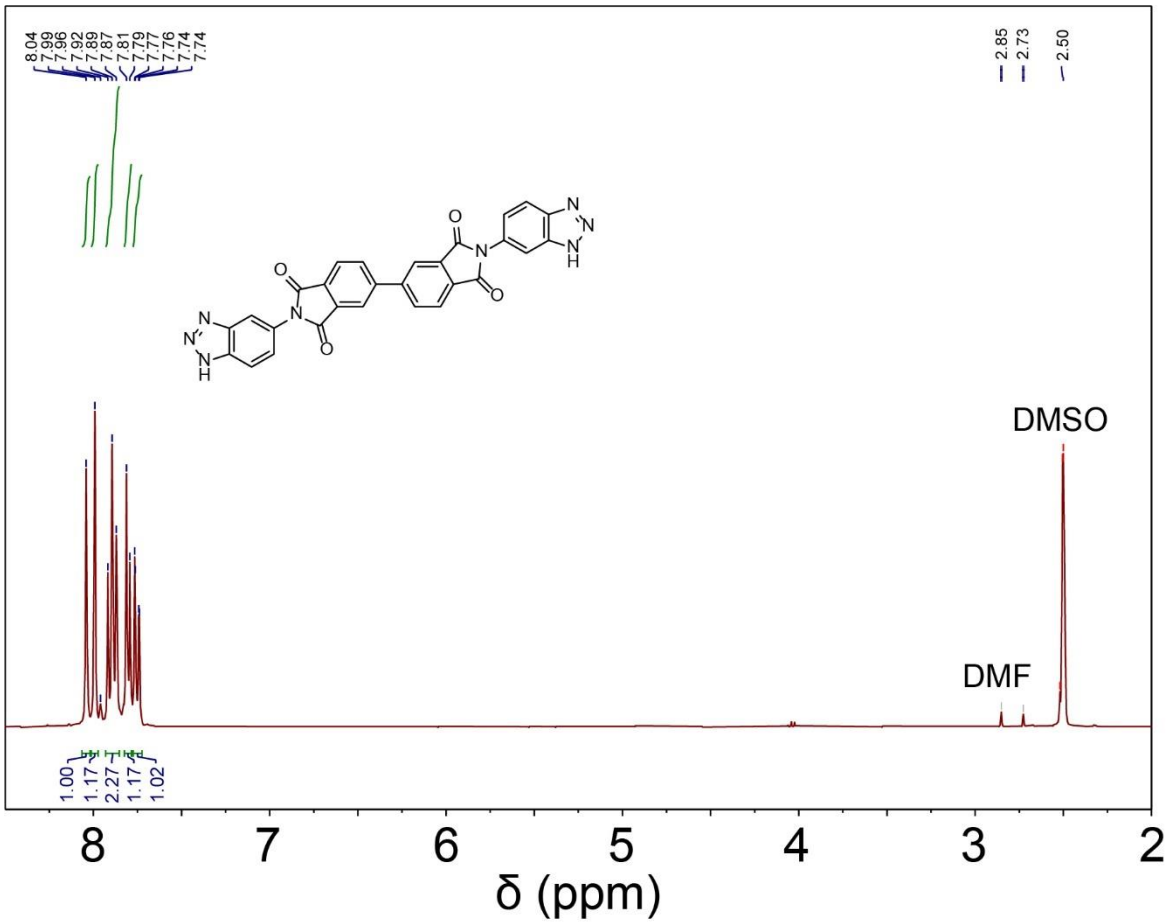

Figure S18. ^{1}H NMR spectrum of H_2bbt-BPDI.
The sample was dissolved in trifluoroacetic acid and several drops of DMSO-d_6 were added to the solution to provide a lock signal for shimming.

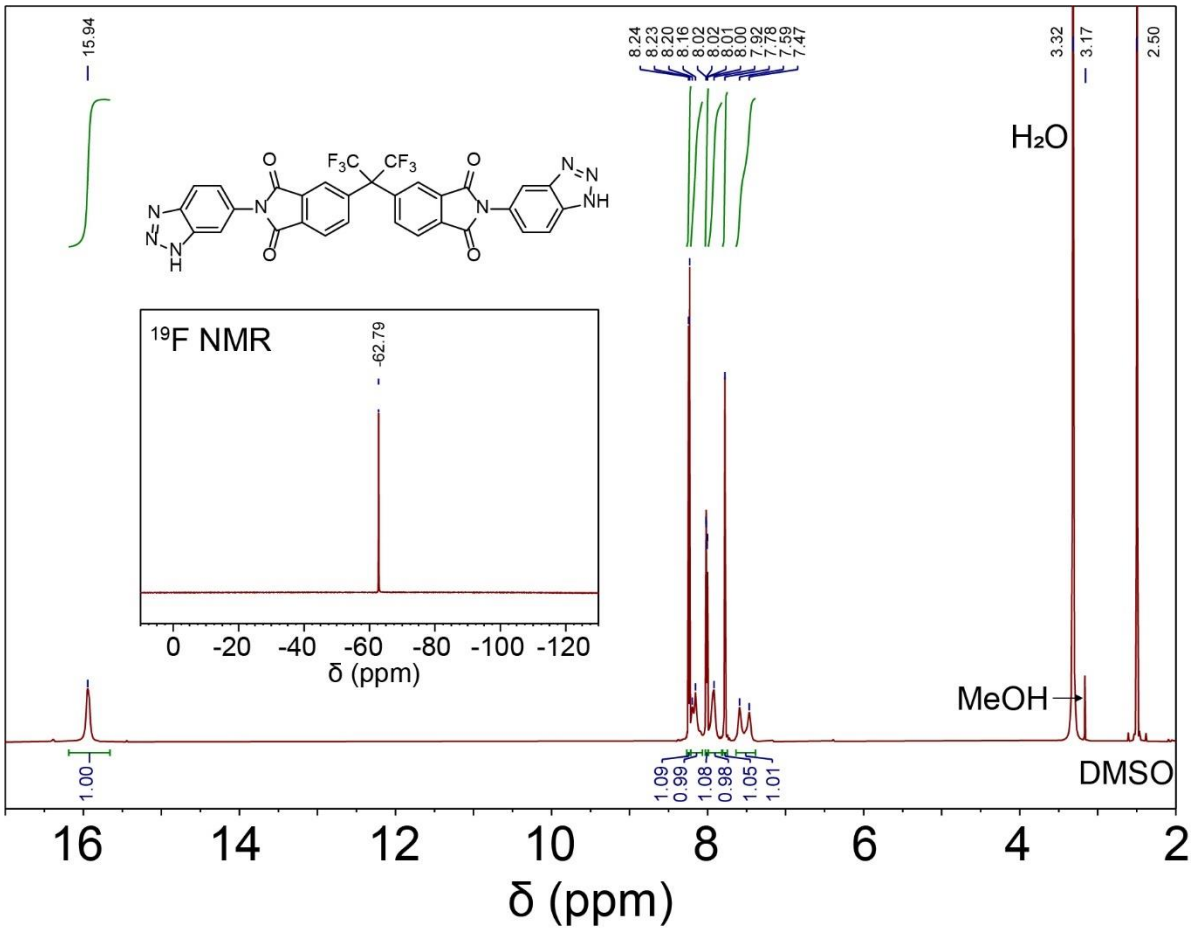

Figure S19. ^{1}H NMR and ^{19}F NMR spectra of H_2bbt-HFIPI.
The sample was dissolved in DMSO-d_6.

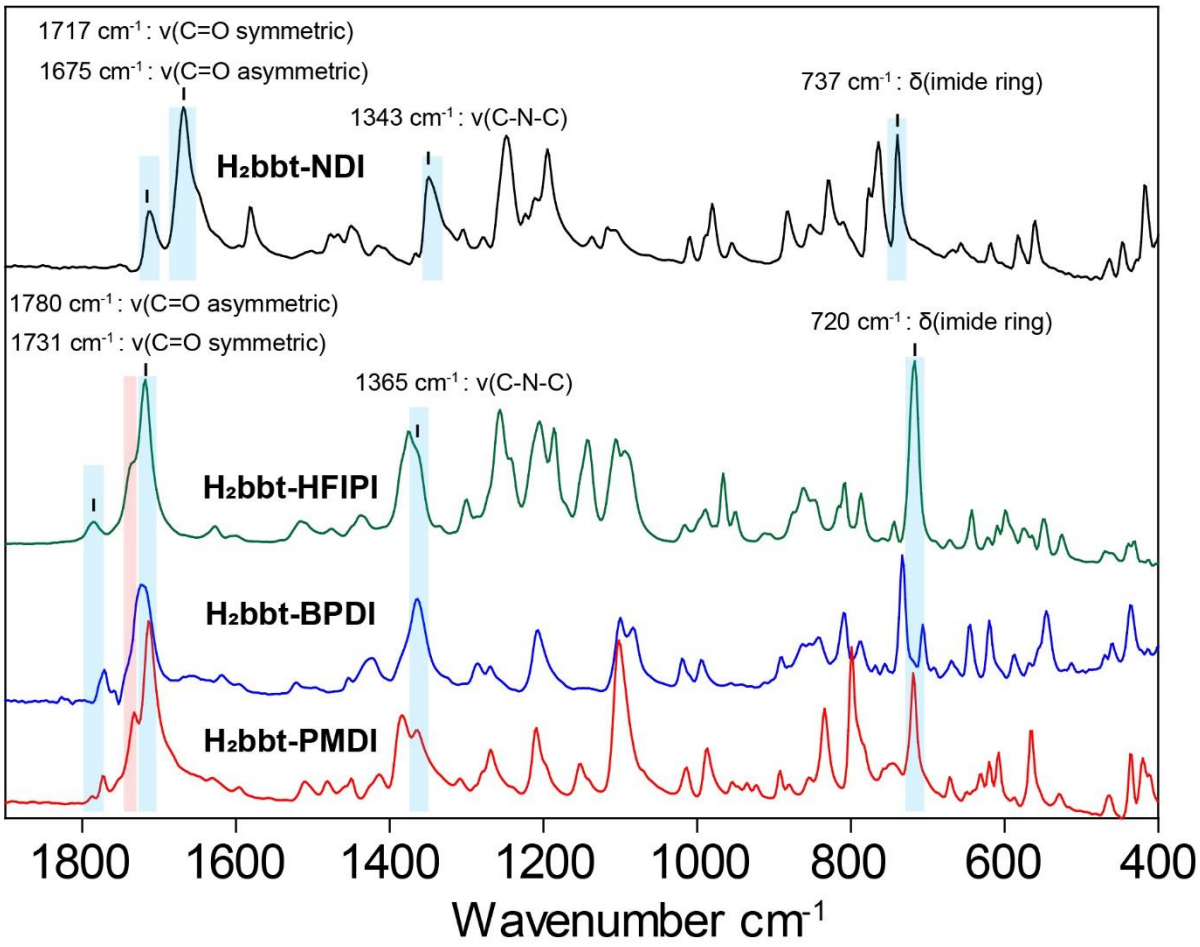

Figure S20. ATR-IR spectra of H_2bbt-XDI linkers (XDI = NDI, HFIPI, BPDI, PMDI). IR bands associated with the imide groups are highlighted in blue and the C=O stretching mode (1732 cm^{-1}) of residual DMF solvent is highlighted in red.

Part 3: Characterization data for 2-XDI MOFs

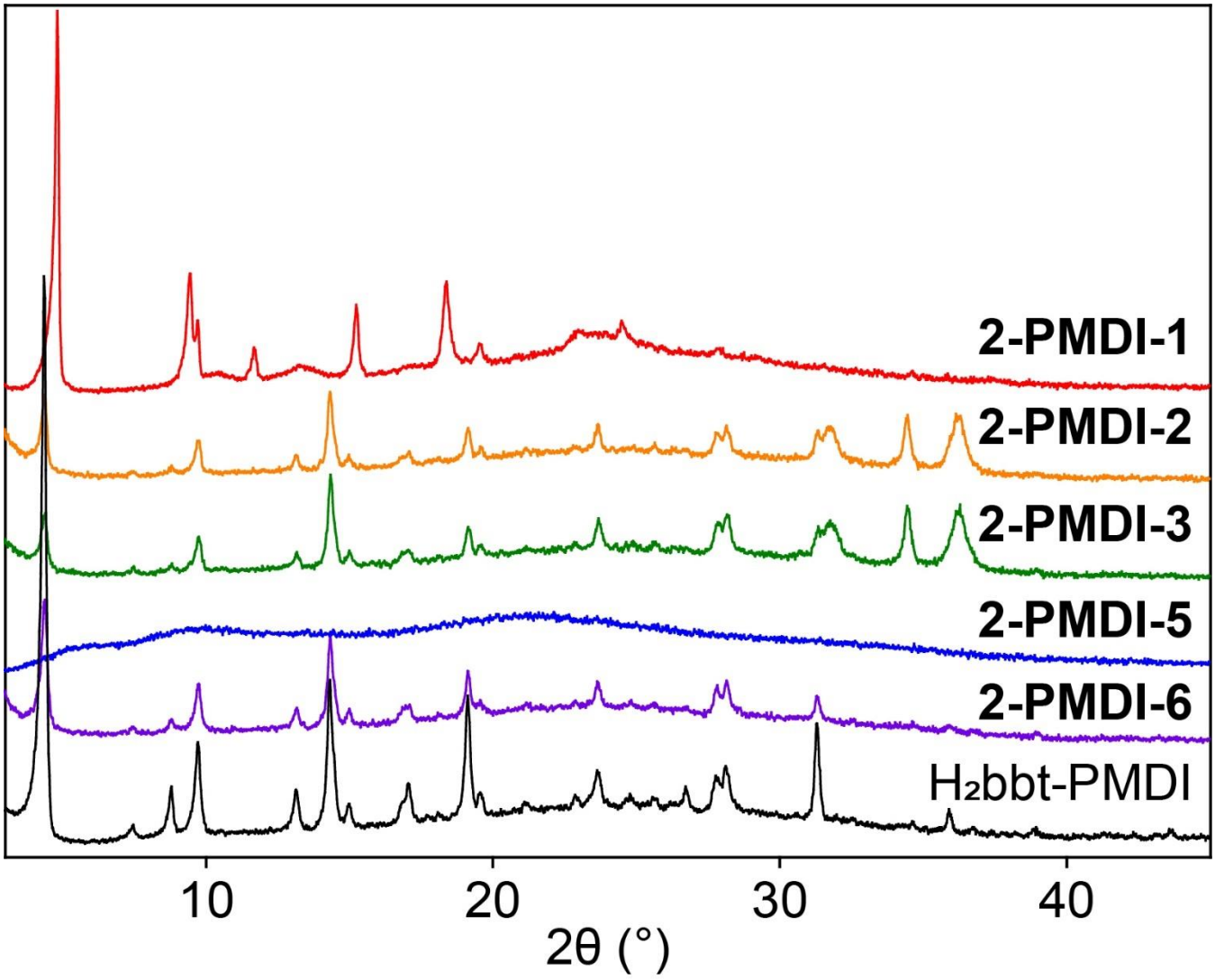

Figure S21. Overlay of the PXRD patterns of solid products obtained from **2-PMDI-n** solvothermal screening reactions.
The overlay shows crystalline H_2bbt-PMDI linker and precipitated solids from solvothermal screening reactions with H_2bbt-PMDI. See Table 1 for the corresponding solvothermal reaction conditions (i.e. **2-PMDI-n**, n = 1-6).

Screening results: Only condition 1 (**2-PMDI-1**) yielded a unique crystalline phase. Conditions 2, 3, and 6 gave the crystalline H_2bbt-PMDI linker phase. Condition 5 yielded an amorphous solid. Condition 1 was used for large scale synthesis and characterization of **2-PMDI**.

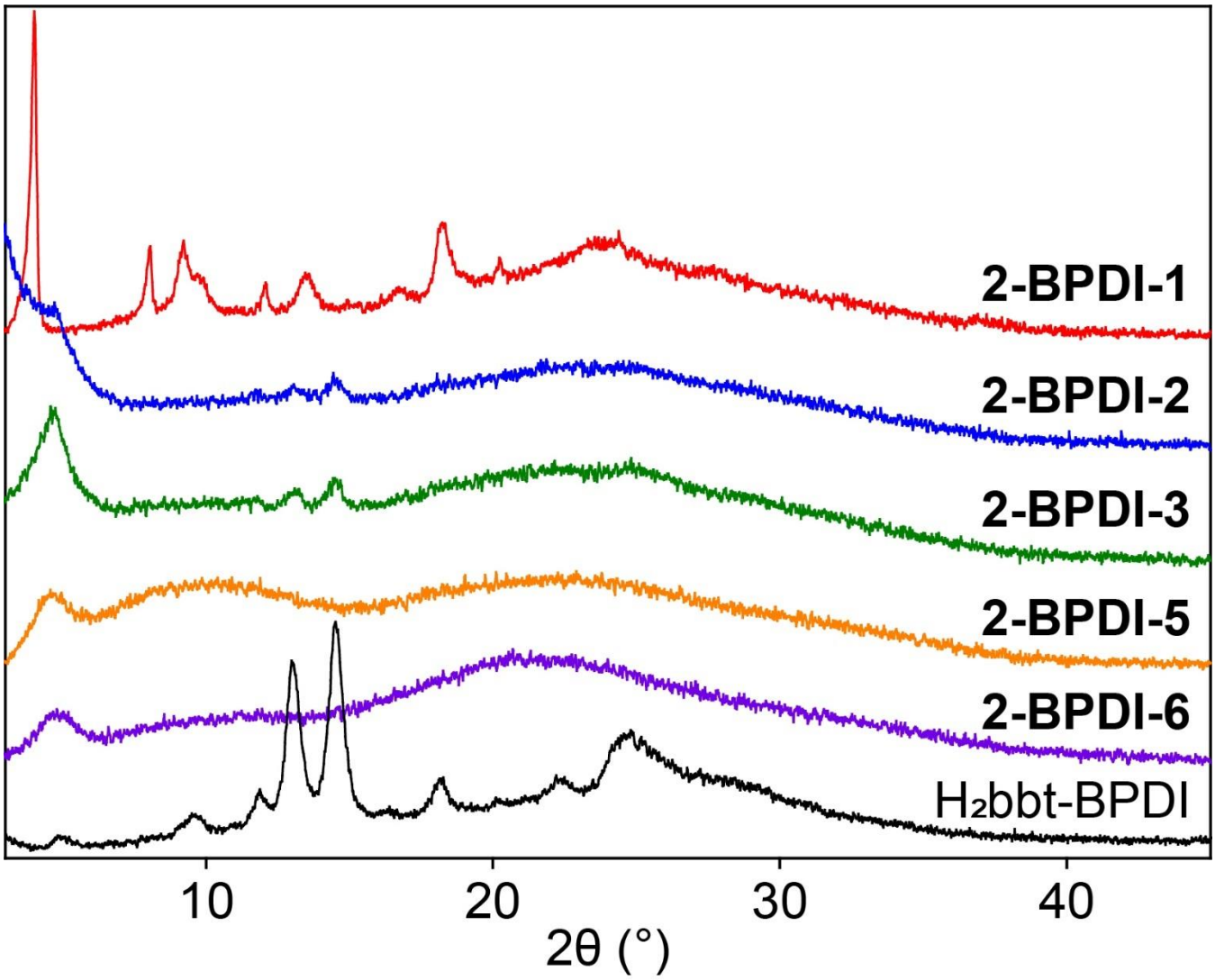

Figure S22. Overlay of the PXRD patterns of solid products obtained from **2-BPDI-n** solvothermal screening reactions.
The overlay shows crystalline H_2bbt-BPDI linker and precipitated solids from solvothermal screening reactions with H_2bbt-BPDI. See Table 1 for the corresponding solvothermal reaction conditions (i.e. **2-BPDI-n**, n = 1-6).

Screening results: A colorless powder was isolated from reaction condition 1 (**2-BPDI-1**) and XRD shows that a poorly crystalline phase is present. The crystalline **H_2bbt-BPDI** linker phase was observed for conditions 2 and 3, and both of the resulting solids had a light orange color. Conditions 5 and 6 yielded flocculent white solids. Condition 1 was chosen for large scale synthesis and characterization of **2-BPDI**.

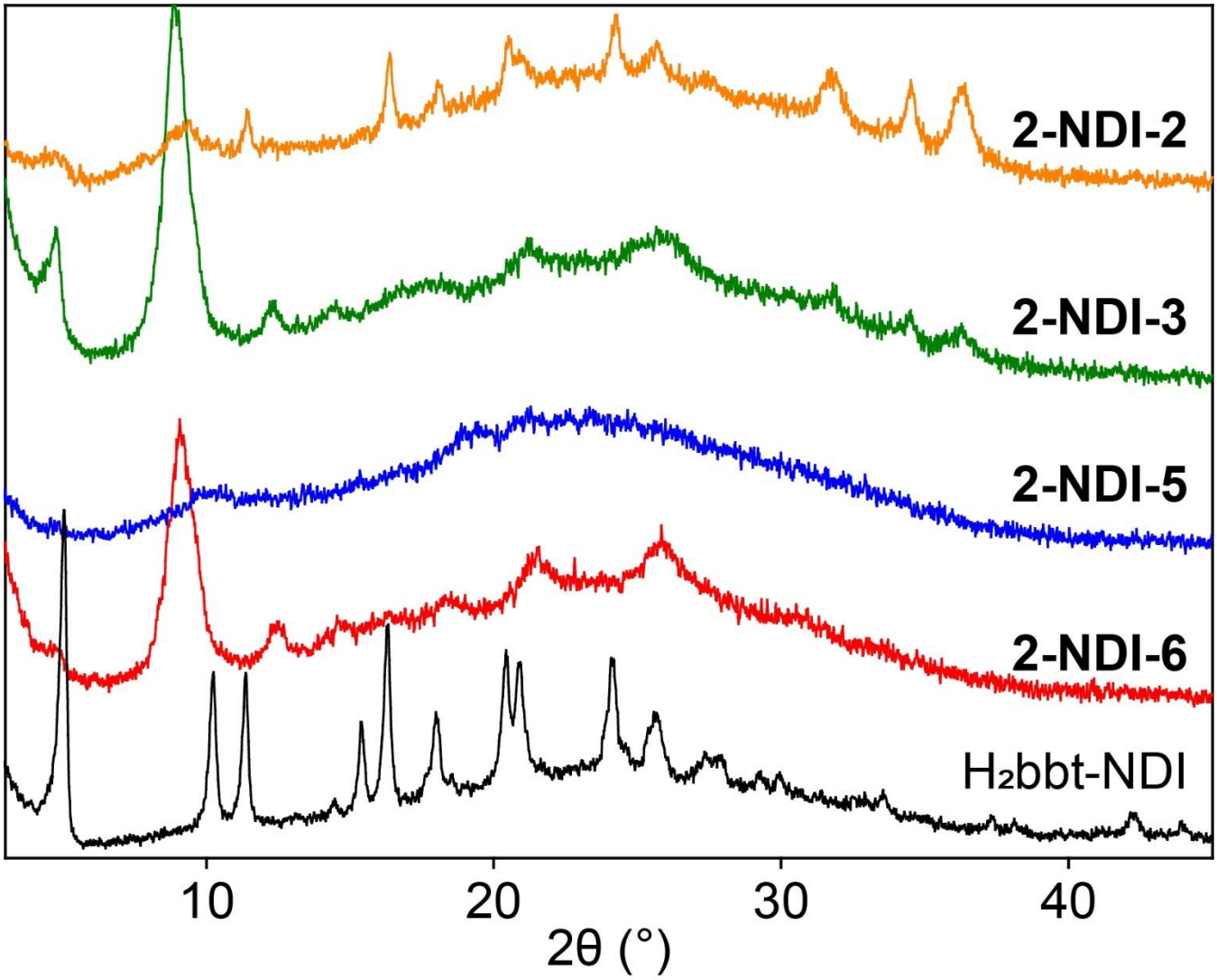

Figure S23. Overlay of the PXRD patterns of solid products obtained from **2-NDI-n** solvothermal screening reactions.
The overlay shows crystalline H_2bbt-NDI linker and precipitated solids from solvothermal screening reactions with H_2bbt-NDI. See Table 1 for the corresponding solvothermal reaction conditions (i.e. **2-NDI-n**, n = 1-6).

Screening results: No solid was observed in reactions using conditions 1 and 4. The crystalline **H_2bbt-NDI** linker phase was observed for condition 2. Conditions 3 and 6 yielded flocculent, dark brown solids that are poorly crystalline. Condition 5 (**2-NDI-5**) yielded a bright yellow solid, although PXRD shows that it is amorphous. Condition 5 was used for large scale synthesis and characterization of the **2-NDI** MOF. Condition 3 and 6 were not chosen for large scale synthesis because the dark brown color of these compounds indicates that the naphthalene diimide groups had been reduced under the solvothermal conditions.[15]

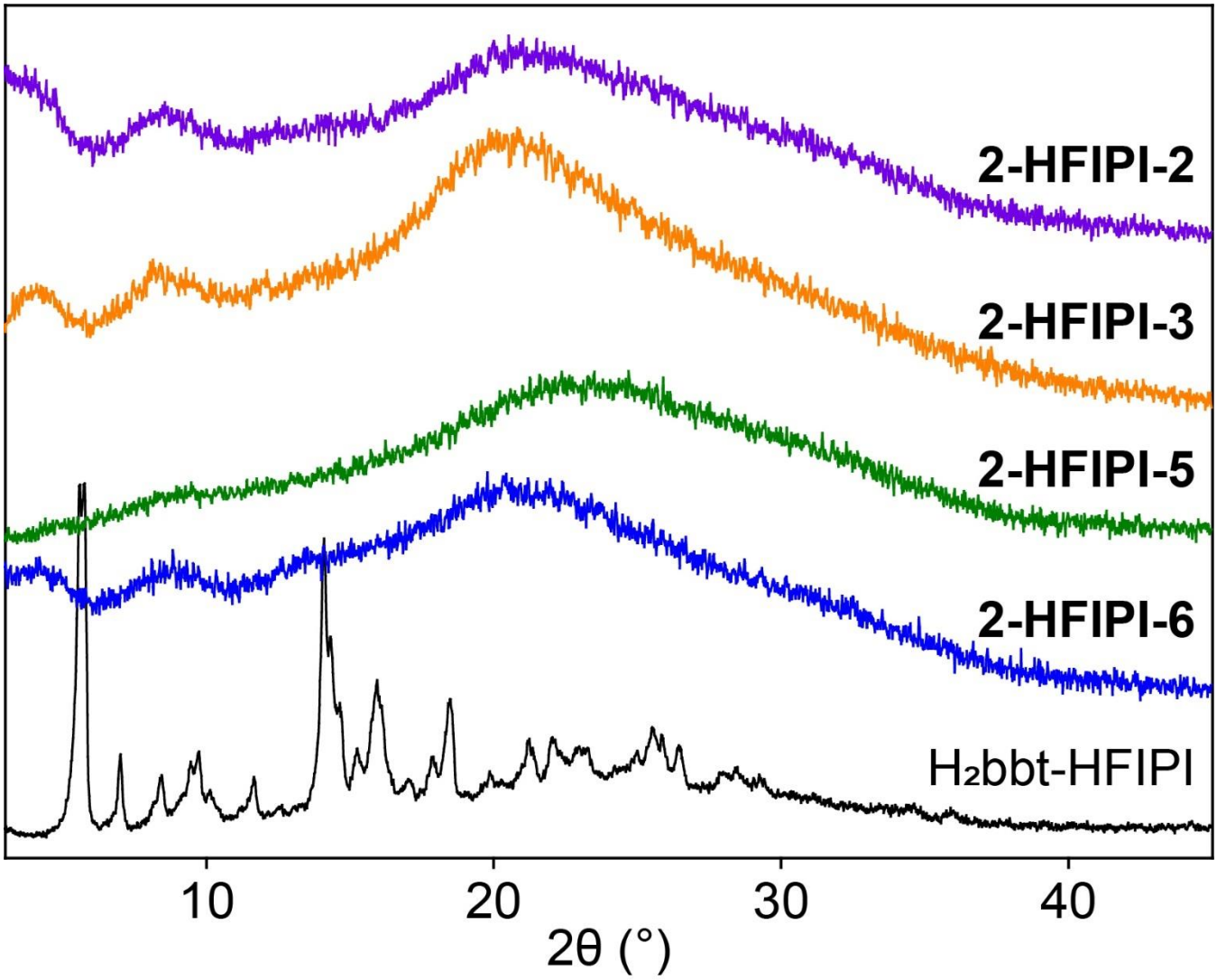

Figure S24. Overlay of the PXRD patterns of solid products obtained from **2-HFIPI-n** solvothermal screening reactions.
The overlay shows crystalline H_2bbt-HFIPI linker and precipitated solids from solvothermal screening reactions with H_2bbt-HFIPI. See Table 1 for the corresponding solvothermal reaction conditions (i.e. **2-HFIPI-n**, n = 1-6).

Screening results: No precipitate was observed for conditions 1 and 4. All other conditions yielded flocculent white solids. None of the resulting solids show the presence of the crystalline **H_2bbt-HFIPI** linker phase. Condition 5 was chosen for large scale synthesis and characterization of **2-HFIPI**. Condition 6 was not chosen since base facilitated the hydrolysis of the **H_2bbt-HFIPI** linker. Conditions 2 and 3 were not chosen since the chloride-based Zn precursor provides a better comparison to the **1-XDI** MOFs which also contains chloride as X-type ligand in the **1-NH_2** clusters.

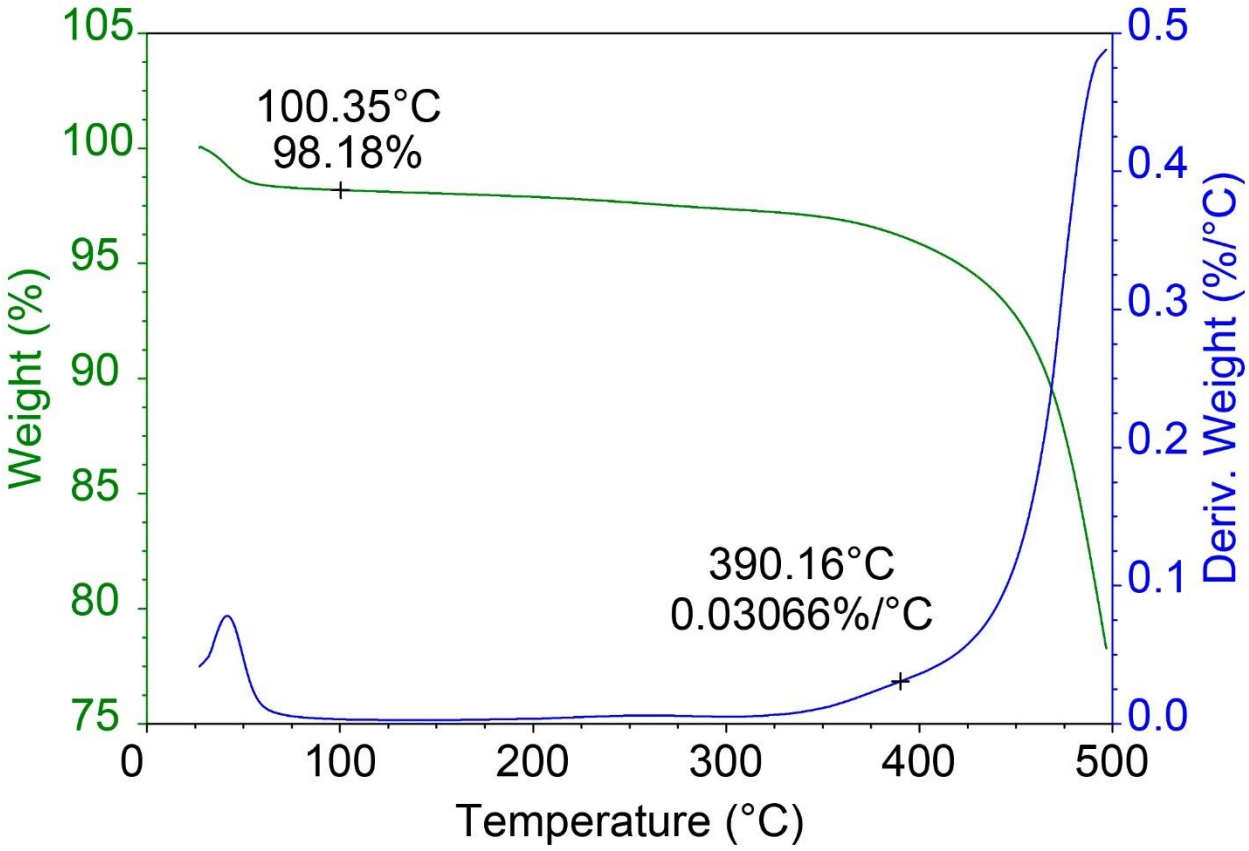

Figure S25. Thermogravimetric analysis data for activated **2-PMDI**.

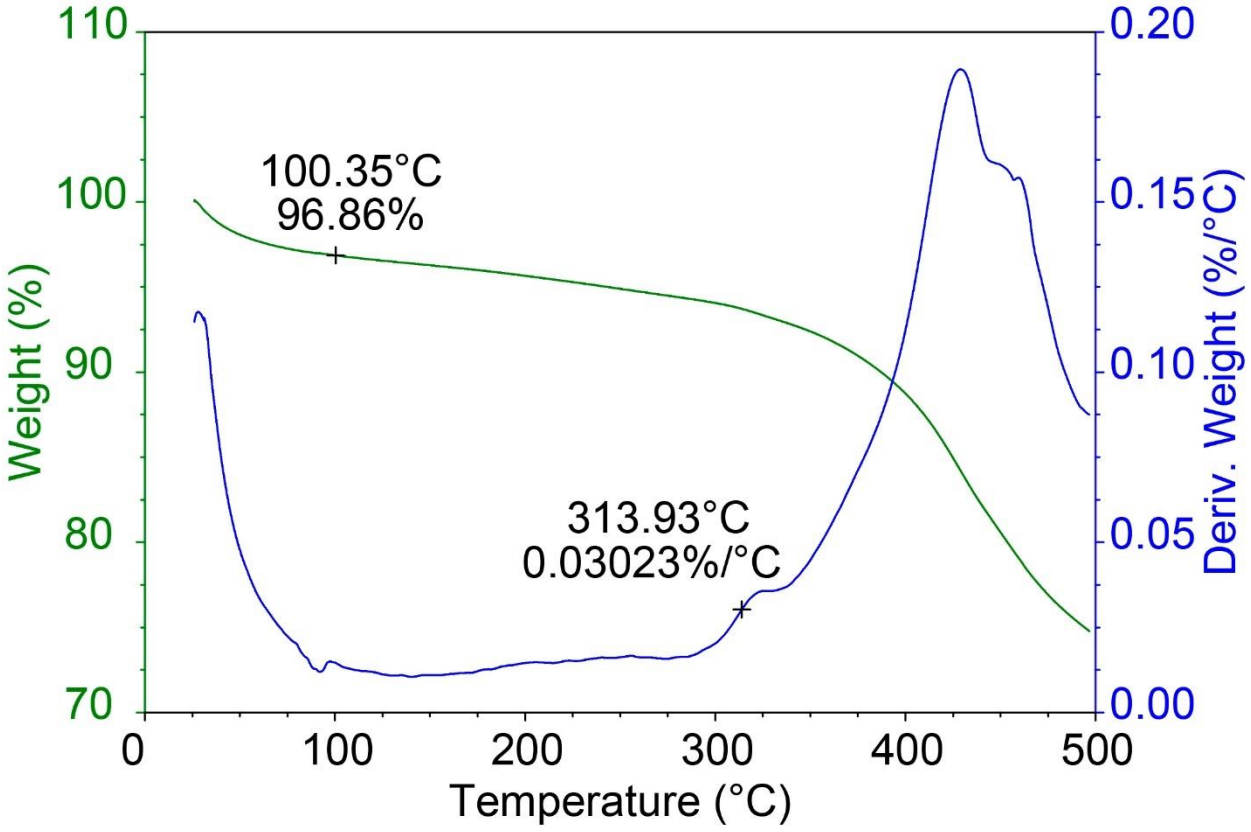

Figure S26. Thermogravimetric analysis data for activated **2-NDI**.

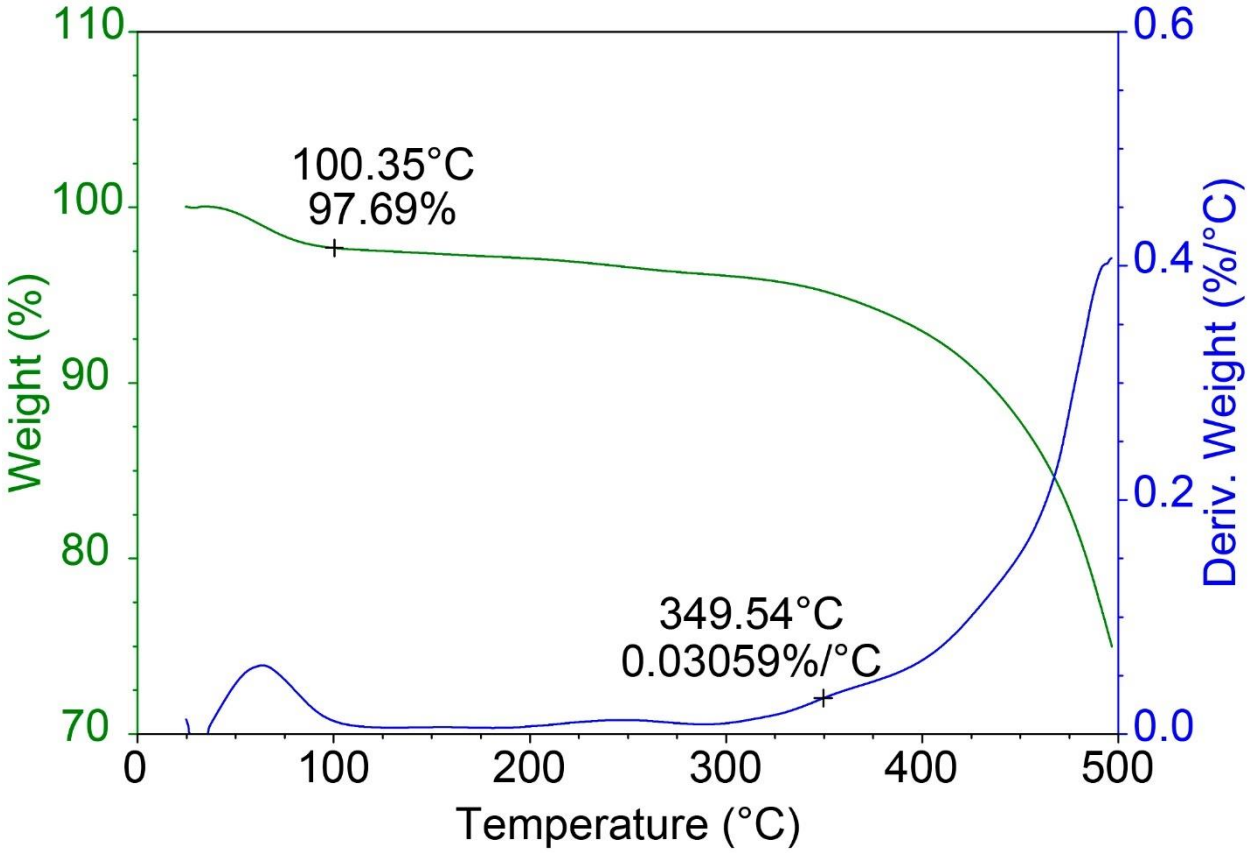

Figure S27. Thermogravimetric analysis data for activated **2-BPDI**.

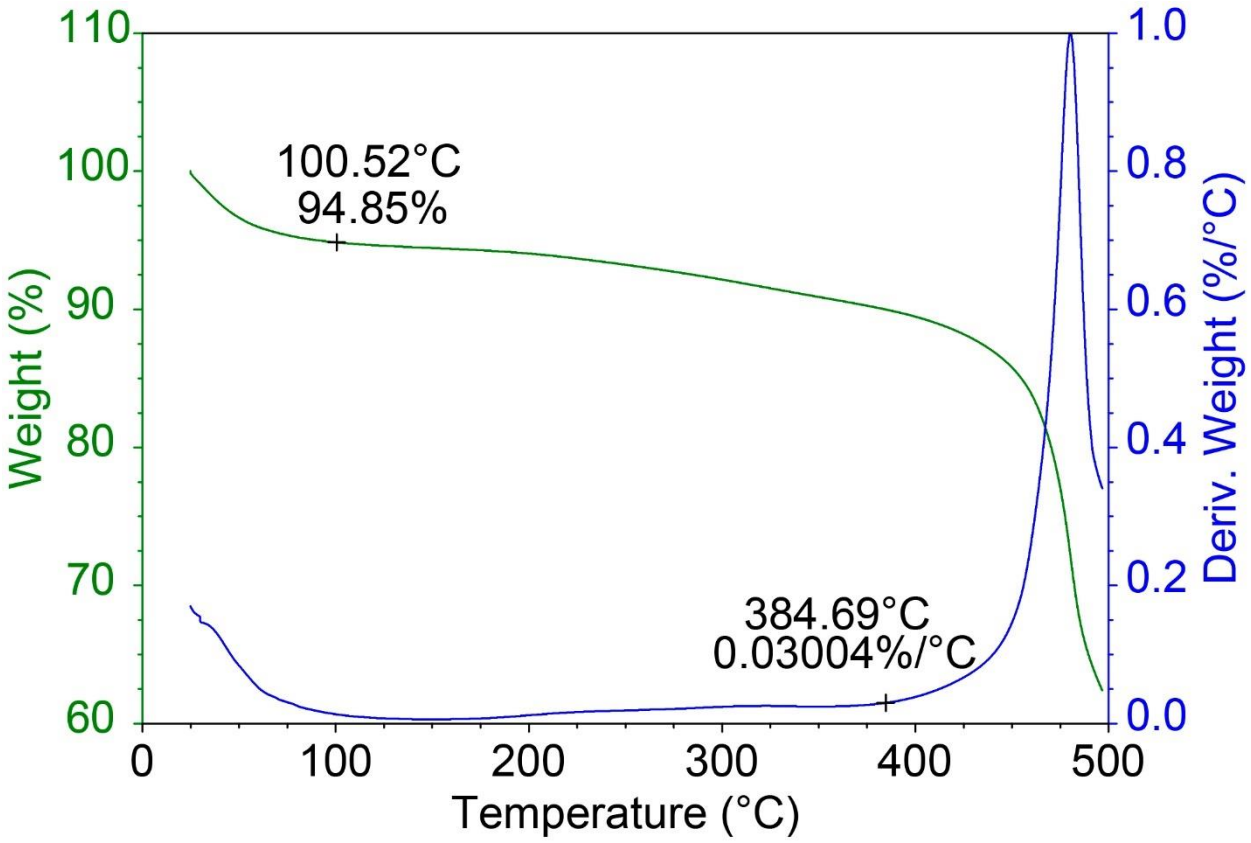

Figure S28. Thermogravimetric analysis data for activated **2-HFIPI**.

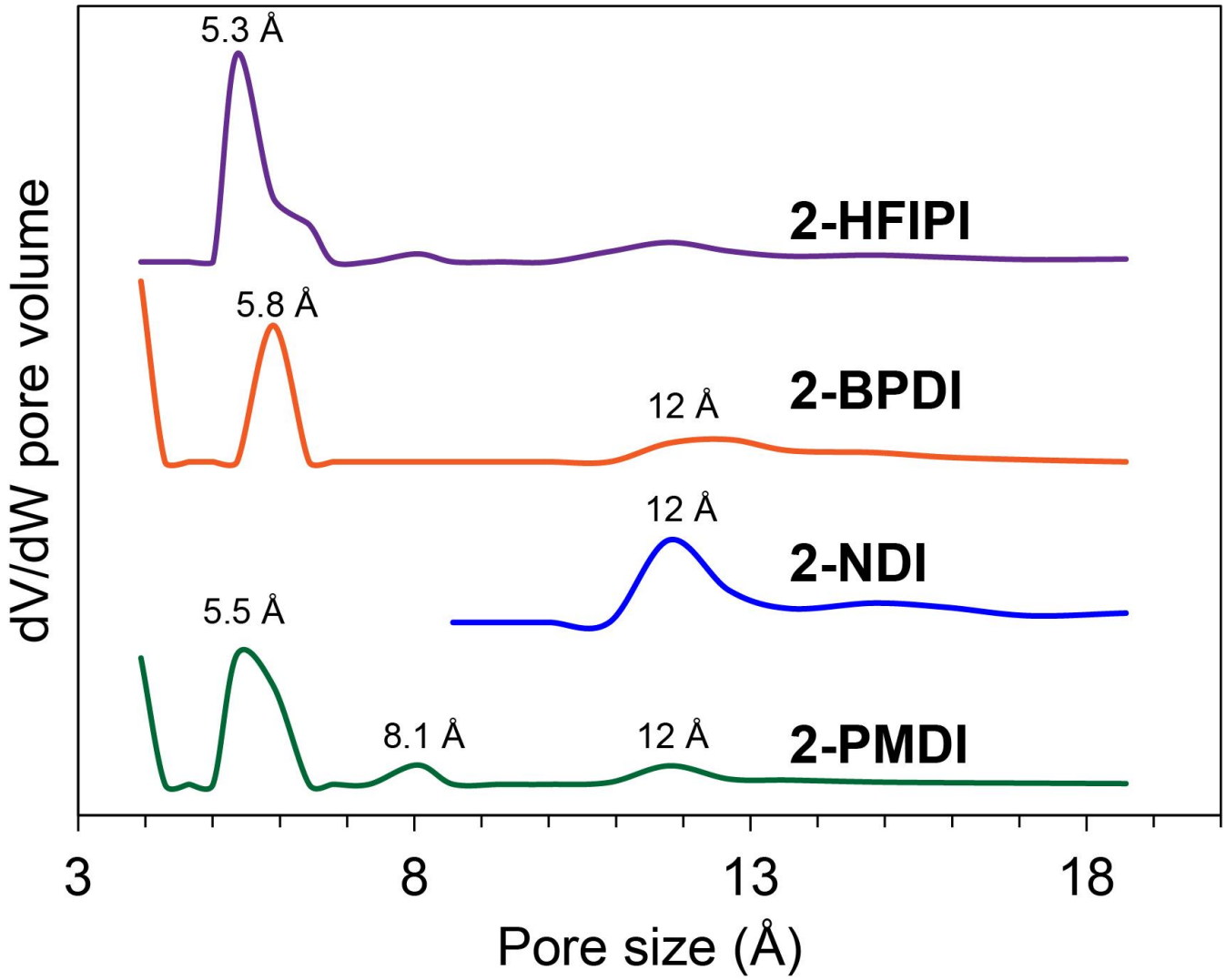

Figure S29. DFT pore size distributions for the **2-XDI** MOFs.

The **2-XDI** MOFs show the presence of small micropores around 5-6 Å and a smaller volume fraction of micropores with ~12 Å diameter. The presence of relatively small micropores and the similarity in pore size distribution for these materials despite the different linker length indicate that they likely adopt interpenetrated structures.

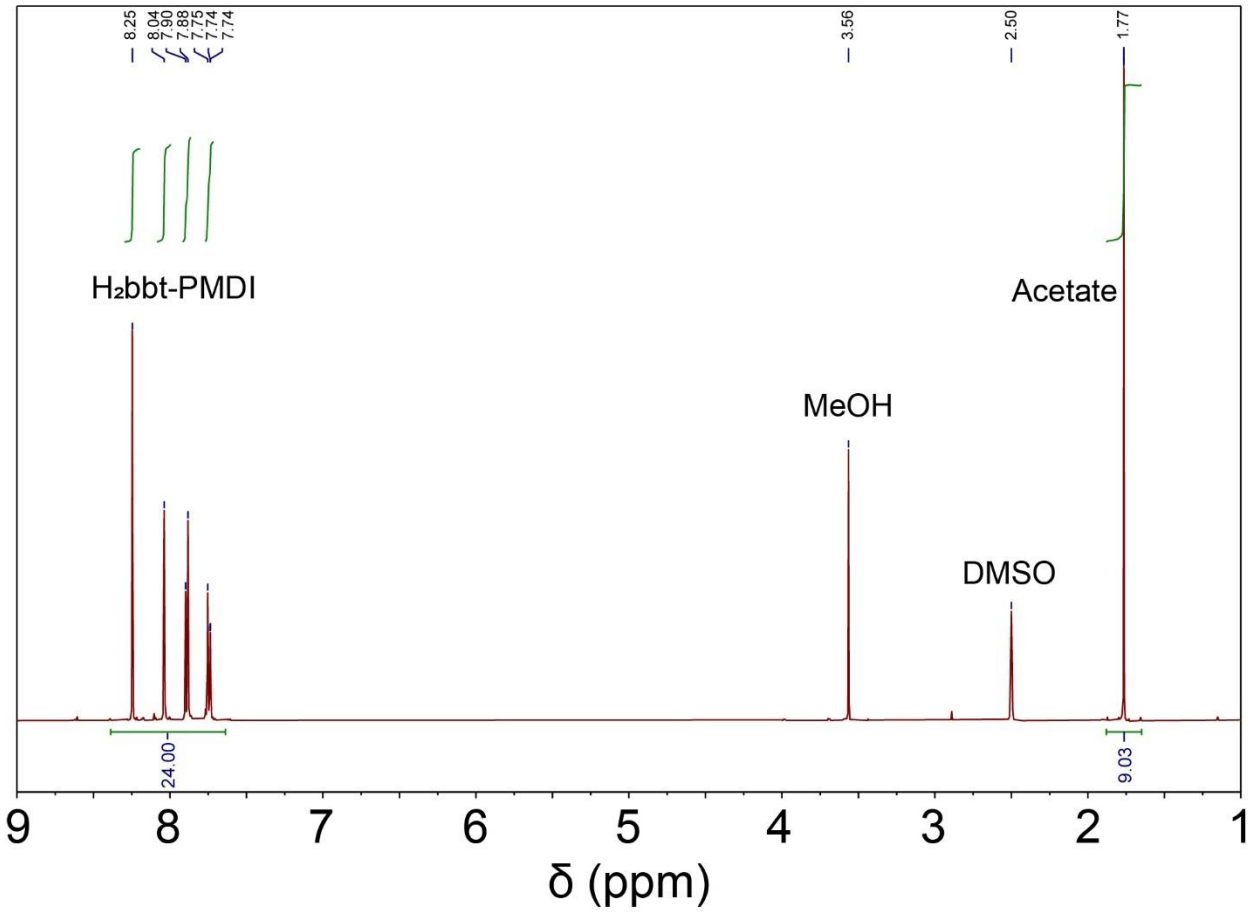

Figure S30. Acid-digested ^{1}H NMR spectrum of **2-PMDI**.

Samples were digested for solution-state ^{1}H NMR analysis by suspending ~5 mg of solid in CF_3CO_2H (1 mL) and gently heating the suspensions until all the solids dissolved. DMSO-d_6 (0.1 mL) was then added to the solutions to provide a lock signal for shimming.

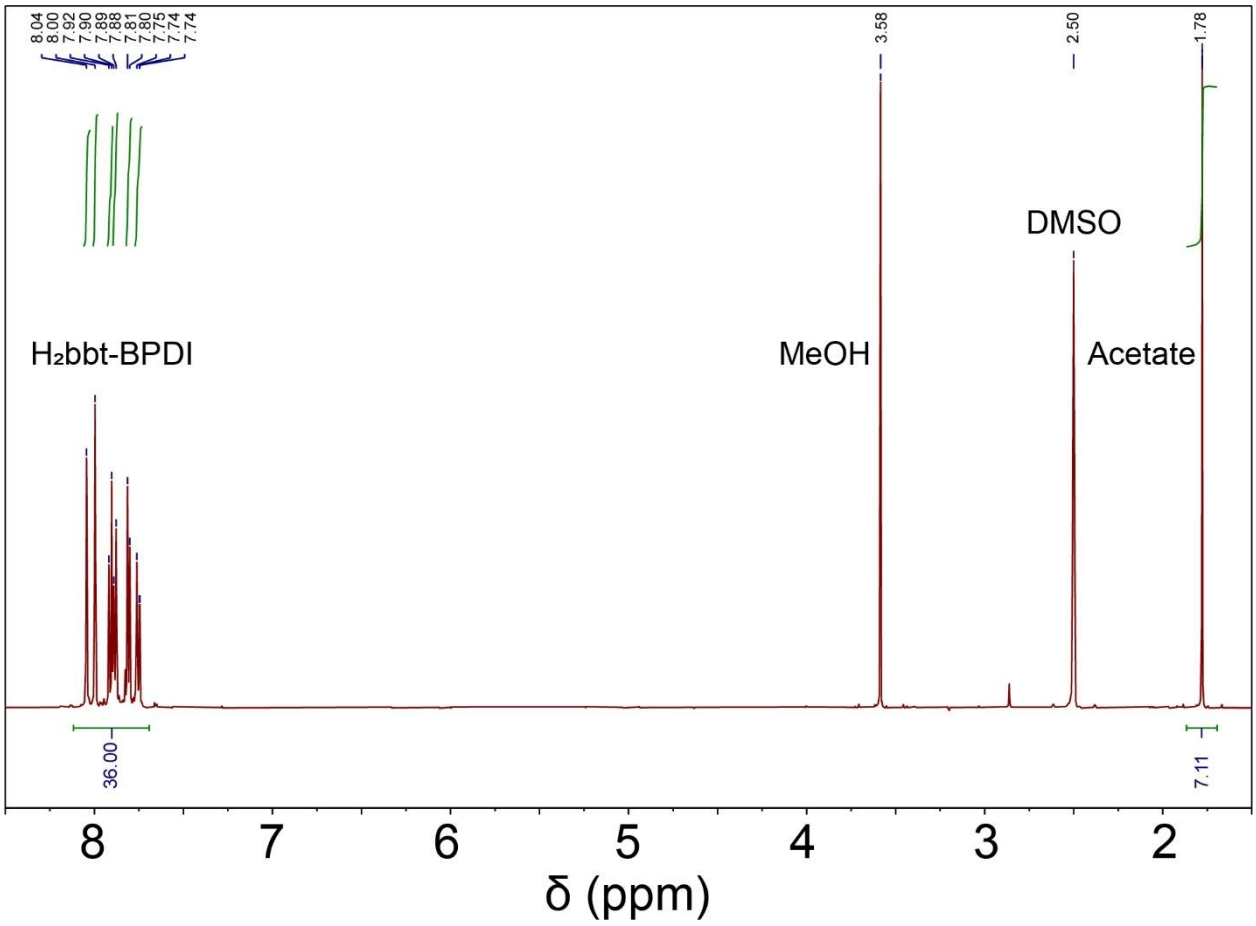

Figure S31. Acid-digested ^{1}H NMR spectrum of **2-BPDI**.

Samples were digested for solution-state ^{1}H NMR analysis by suspending ~5 mg of solid in CF_3CO_2H (1 mL) and gently heating the suspensions until all the solids dissolved. DMSO-d_6 (0.1 mL) was then added to the solutions to provide a lock signal for shimming.

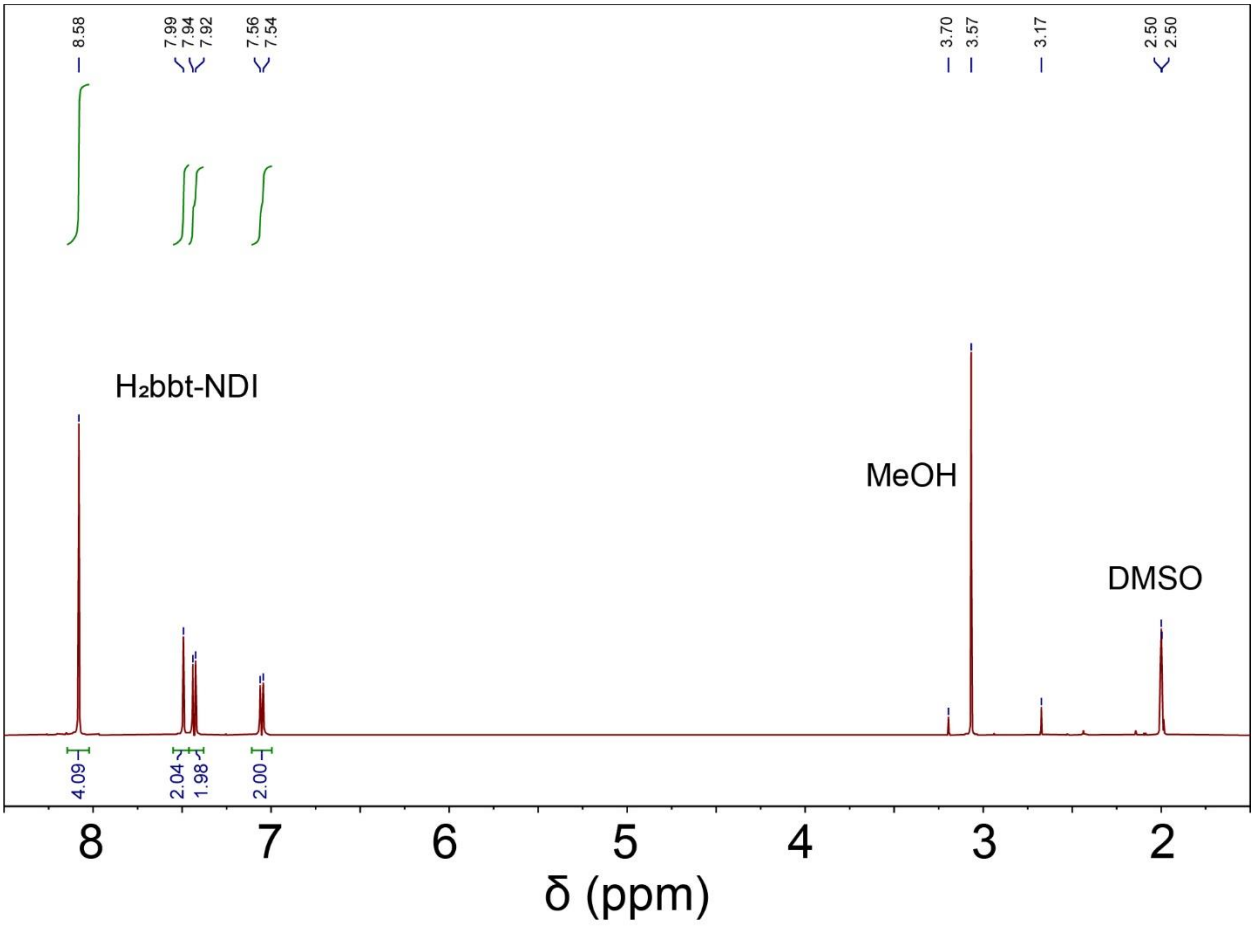

Figure S32. Acid-digested ^{1}H NMR spectrum of **2-NDI**.

Samples were digested for solution-state ^{1}H NMR analysis by suspending ~5 mg of solid in CF_3CO_2H (1 mL) and gently heating the suspensions until all the solids dissolved. DMSO-d_6 (0.1 mL) was then added to the solutions to provide a lock signal for shimming.

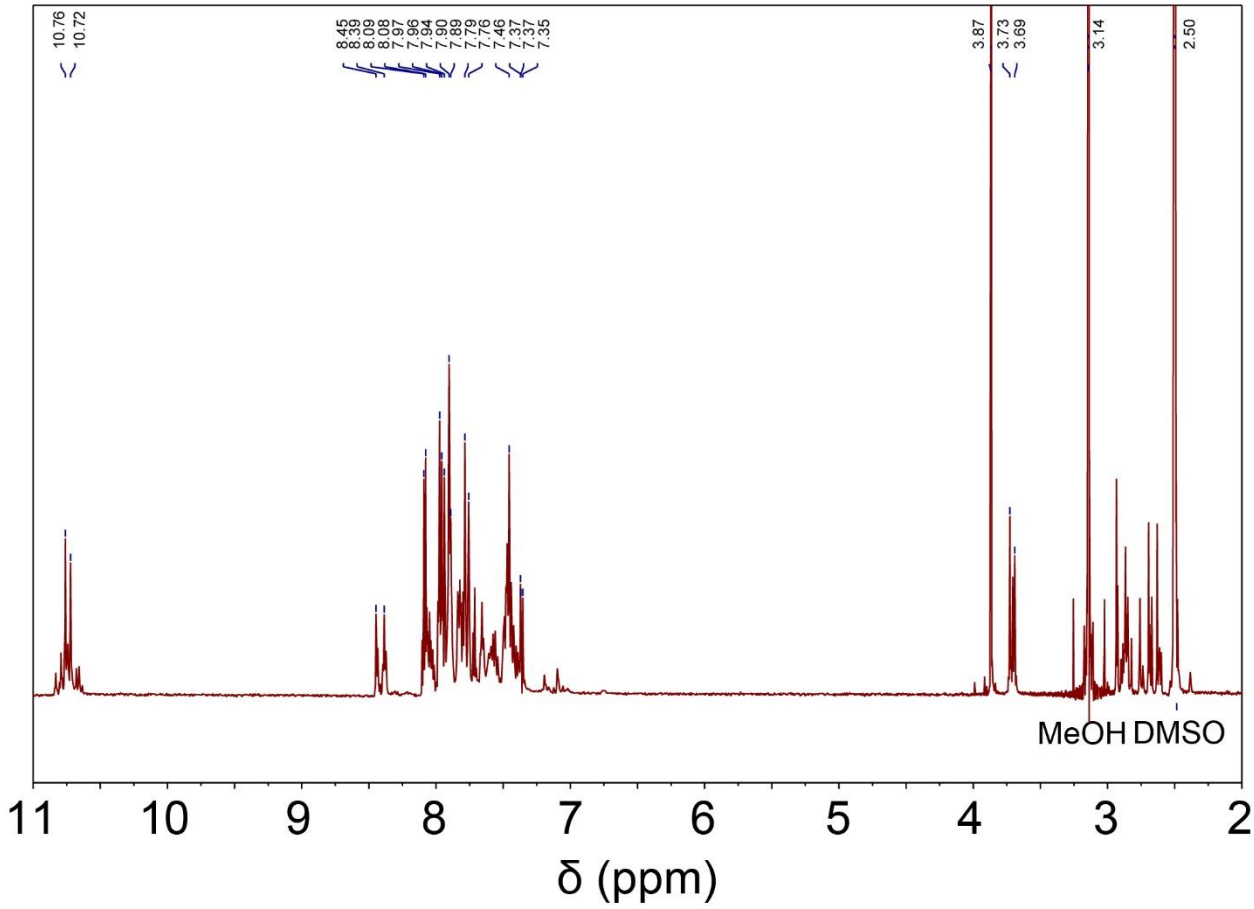

Figure S33. Acid-digested ^{1}H NMR spectrum of **2-HFIPI**.

Samples were digested for solution-state ^{1}H NMR analysis by suspending ~5 mg of solid in CF_3CO_2H (1 mL) and gently heating the suspensions until all the solids dissolved. DMSO-d_6 (0.1 mL) was then added to the solutions to provide a lock signal for shimming.

The bbt-HFIPI^{2-} linkers undergo hydrolysis to form amide/carboxylate species during the MOF solvothermal synthesis reaction. As a result, the H_2bbt-HFIPI diimide species are not clearly observed in the ^{1}H NMR spectrum. The ATR-IR spectrum of **2-HFIPI** (Figure S34) confirms the presence of hydrolyzed linkers species as the major products.

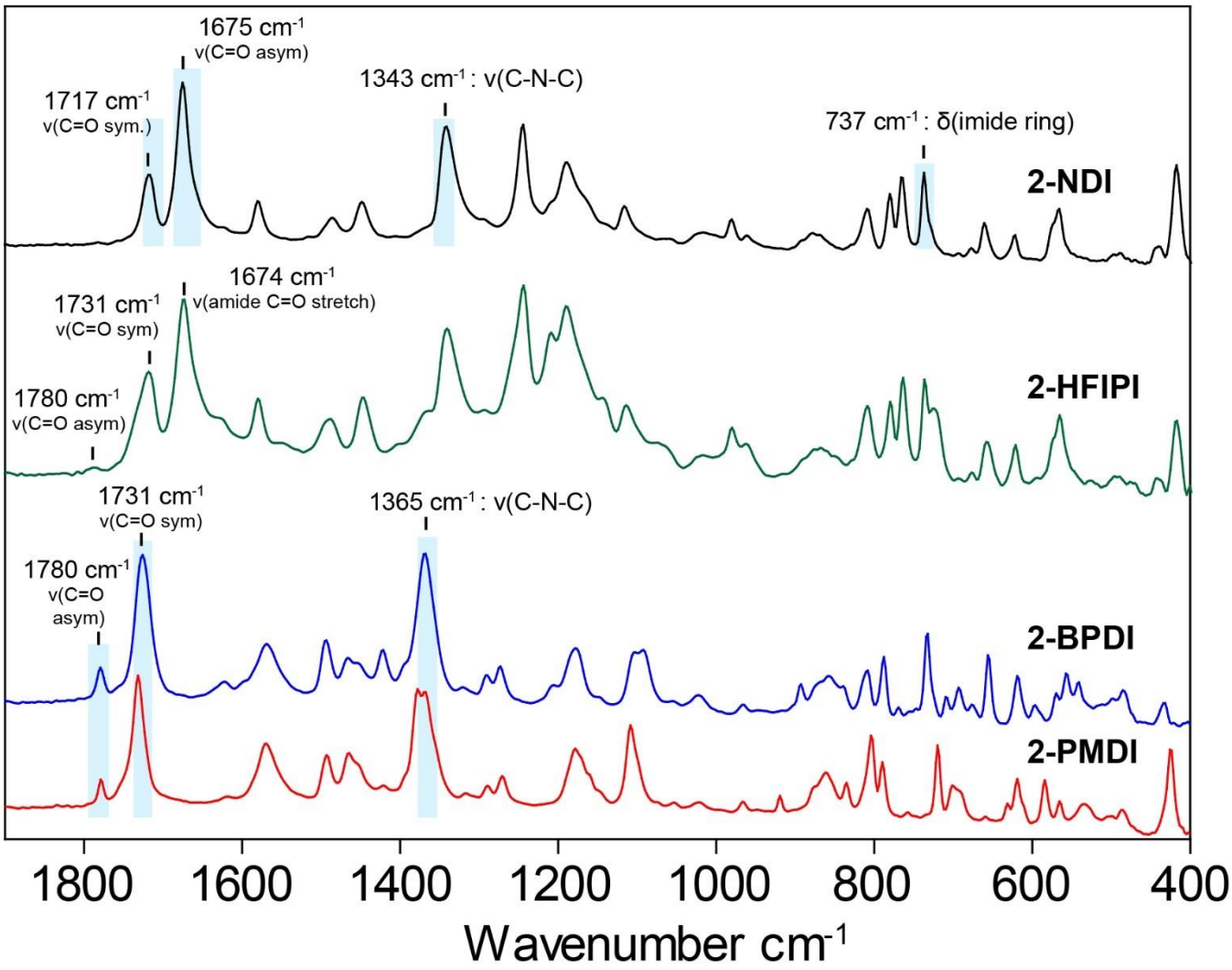

Figure S34. ATR-IR spectra of **2-XDI** MOFs.
IR bands associated with the imide groups are highlighted in blue.

Part 4: Attempted structural characterization of crystalline 1-PMDI and 2-XDI samples.

PXRD data for **2-PMDI**, **2-BPDI** and **1-PMDI** (Figure S35) were obtained using a Bruker D8 Advance powder diffractometer (Cu Kα radiation, λ = 1.5418 Å). The TOPAS-Academic (version 6) software package was used to attempt to index the patterns. Owing to the poor crystallinity of **1-PMDI**, we were unable to select a suitable number of reflections for indexing, hindering any further analysis of the data. For **2-PMDI** and **2-BPDI**, less than 20 reflections were found to be suitable for indexing each pattern and the unit cells could not be identified with any reasonable degree of confidence. Based on the estimated linker lengths and Zn···Zn distances (Table S12 and Figure S36), the unit cell volumes could be larger than 50,000 $Å^3$. PXRD indexing software such as Topas is typically only capable of generating results with cell volumes smaller than 20,000 $Å^3$. Consequently, we attempted to determine the structures of **1-PMDI**, **2-PMDI**, and **2-BPDI** using Micro-Electron Diffraction (Micro-ED, Figure S37). The TEM images show irregular shaped particles that tended to aggregate and ranged in size from 100 nm to 1 μm. Over 40 particles were inspected for each sample, but well-defined single crystallites could not be located. Electron diffraction patterns of the particles showed weak diffraction and/or smearing of the reflections indicative of a polycrystalline particle.

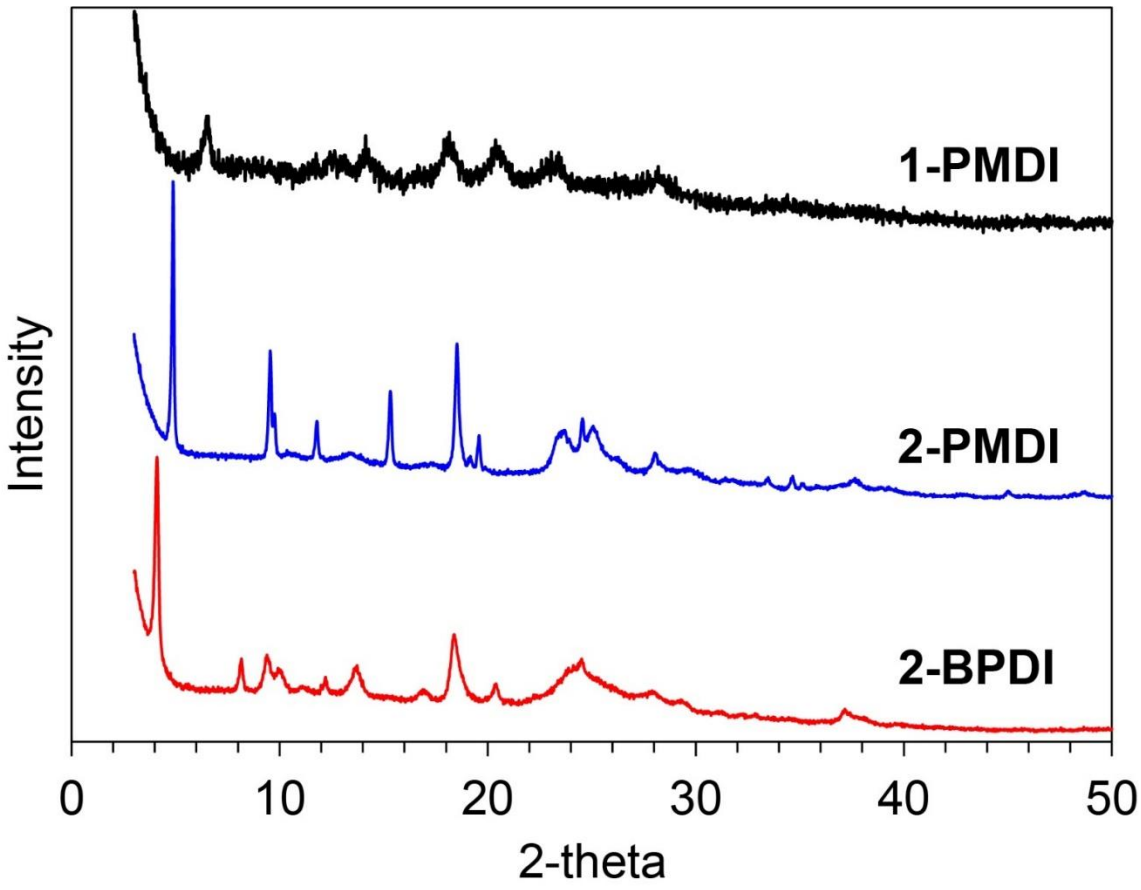

Figure S35. Overlay of PXRD patterns measured for **1-PMDI**, **2-PMDI**, and **2-BPDI**.

Table S12. Correlation between the Zn_c–Zn_c distance and the unit cell volume in **2-PMDI**, **2-BPDI**, and some known bis-benzotriazolate-based MOFs.

Benzotriazolate MOF name	Zn_c–Zn_c distance (Å)	Space group	Unit cell volume (Å^3)	References
MFU-4	10.8	*F* m̄ 3 m̄	10114	[16]
MFU-4*l*	15.5	*F* m̄ 3 m̄	29955	[17]
CFA-7	20.4	*R*-3 m	49704	[18]
2-PMDI	21.86-22.60	Unknown	Unknown	-
2-BPDI	20.55-25.86	Unknown	Unknown	-

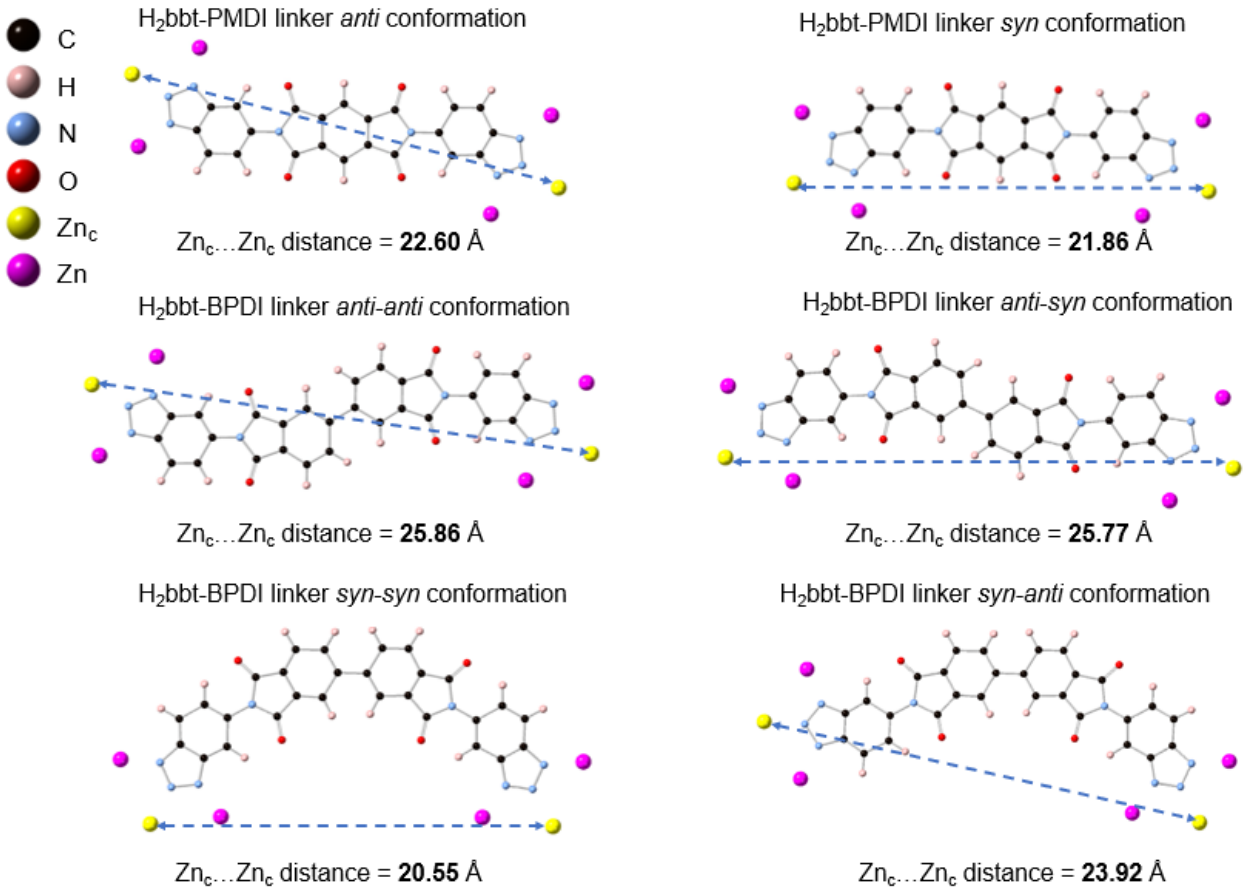

Figure S36. Possible linker conformations and estimated Zn···Zn distances for **2-PMDI** and **2-BPDI** MOFs.

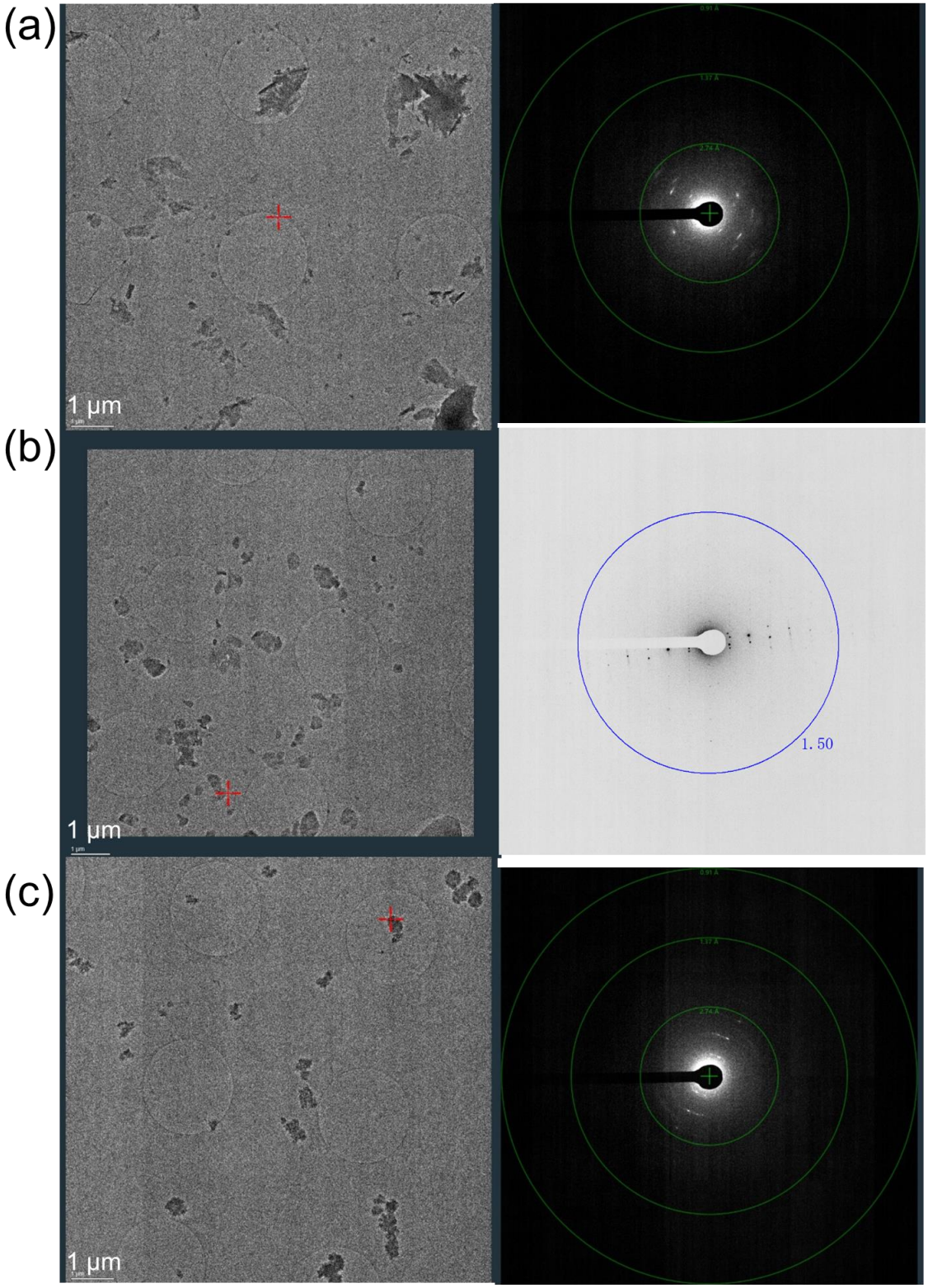

Figure S37. TEM image (left) and electron diffraction images (right) of selected crystals of (a) **1-PMDI**, (b) **2-PMDI** and (c) **2-BPDI** MOFs and with improved sample preparation.

Part 5: Gas adsorption data and binary gas mixture selectivity for 1-XDI and 2-XDI MOFs.

Table S13. Predicted IAST selectivity for binary equimolar gas mixtures (1 bar, 300 K) for the **1-XDI** MOFs.

Sample/Gas	C_2H_2/CO_2	C_2H_4/C_2H_6*	C_3H_6/C_3H_8
1-PMDI	1.5	-	2.8
1-NDI	2.8	-	1.8
1-BPDI	2.3	-	1.7
1-HFIPI	2.9	-	1.9
*The isotherm data for the **1-XDI** MOFs do not display any selectivity for C_2H_4/C_2H_6 separation, so the IAST selectivity values have not been calculated.			

Table S14. Predicted IAST selectivity for binary equimolar gas mixtures (1 bar, 300 K**)** for the **2-XDI** MOFs.

Sample/Gas	C_2H_2/CO_2	C_2H_4/C_2H_6	C_3H_6/C_3H_8
2-PMDI	3.4	2.4	10.5
2-NDI	3.3	1.1	2.6
2-BPDI	2.3	1.3	6.0
2-HFIPI	2.6	1.3*	1.5
***2-HFIPI** shows a slight inverse selectivity for adsorption of C_2H_6 over C_2H_4, and the corresponding C_2H_6/C_2H_4 selectivity value is listed in the table.			

Table S15. Adsorption capacities (mmol/g) at 1 bar for C_1-C_3 gases in **1-XDI** MOFs.[a]

Sample/Gas	CO_2	C_2H_2	C_2H_4	C_2H_6	C_3H_6	C_3H_8
1-PMDI	0.27	0.30	0.09	0.07	0.11	0.07
1-NDI	1.38	1.79	1.21	1.16	1.78	1.53
1-BPDI	1.32	1.63	1.20	1.18	1.68	1.42
1-HFIPI	1.45	1.89	1.32	1.27	1.77	1.47

Table S16. Adsorption capacities (mmol/g) at 1 bar for C_1-C_3 gases in **2-XDI** MOFs.[a]

Sample/Gas	CO_2	C_2H_2	C_2H_4	C_2H_6	C_3H_6	C_3H_8
2-PMDI	1.36	1.31	1.04	0.89	1.11	0.90
2-NDI	1.09	1.31	0.85	0.76	1.24	0.94
2-BPDI	1.33	1.63	1.24	1.11	1.62	1.32
2-HFIPI	1.46	1.87	1.25	1.43	1.90	1.67

[a] Uptake (mmol/g) at 300 K and 1 bar.

Table S17. Summary of gas adsorption properties and C_3H_6/C_3H_8 selectivity of some reported MOFs.

MOF Material	C_3H_6 Capacity (mmol/g)	C_3H_8 Capacity (mmol/g)	Capacity C_3H_6/C_3H_8	IAST selectivity	Reference
1-NDI	1.78	1.53	1.2	1.8	-
1-BPDI	1.68	1.42	1.2	1.7	-
1-HFIPI	1.77	1.47	1.2	1.9	-
2-PMDI	1.11	0.90	1.2	10.5	-
2-NDI	1.24	0.94	1.3	2.6	-
2-BPDI	1.62	1.32	1.2	6.0	-
2-HFIPI	1.90	1.67	1.1	1.5	-
$Zn_9(OH)_6(bbtm)_6$	4.08	3.49	1.2	1.1	19
AGTU-3a	1.22	0.46	2.7	7.0	20
MAF-23-O	1.38	1.02	1.3	8.8	21
Ni-NP	3.57	2.13	1.7	10.5	22
Ni-MOF-74	4.85	4.00	1.2	10	23
Mn_2(m-dobdc)	7.23	5.92	1.2	43	24
Fe_2(m-dobdc)	7.31	5.92	1.2	60	24
Co_2(m-dobdc)	7.55	6.04	1.3	38	24
Ni_2(m-dobdc)	7.33	6.06	1.2	35	24
Co-gallate	1.79	0.14	12.8	333	25
UTSA-400	4.42	0.12	36.8	$>10^7$	26

[#] all reported conditions are under 298 K and 1 bar, equimolar selectivity.

Table S18. Summary of gas adsorption properties and C_2H_2/CO_2 selectivity of some reported MOFs.

MOF or Polymer Material	CO_2 Capacity (mmol/g)	C_2H_2 Capacity (mmol/g)	Capacity C_2H_2/CO_2	IAST selectivity	Reference
1-NDI	1.38	1.79	1.3	2.8	-
1-BPDI	1.32	1.63	1.2	2.3	-
1-HFIPI	1.45	1.89	1.3	2.9	-
2-PMDI	1.36	1.31	1.0	3.4	-
2-NDI	1.09	1.31	1.2	3.3	-
2-BPDI	1.33	1.63	1.2	2.3	-
2-HFIPI	1.46	1.87	1.3	2.6	-
CuI@UiO-66-$(COOH)_2$	1.70	2.31	1.4	185.0	27
Cu_2(ATC) (ATC-Cu)	4.02	5.01	1.2	53.6	28
Ni_2(L-mal)$_2$(bpy) (MOF-OH)	1.20	3.04	2.5	25.0	29
Ni_2(L-asp)$_2$(bpy) (MOF-NH_2)	1.40	2.67	1.9	12.5	29
$[Ni_2(OH)(H_2O)_2Pz_3]_n$ (BUT-85)	1.28	2.95	2.3	6.1	30
$Zn_5(bbta)_3F_{2.11}Cl_{1.22}OH_{0.67}$ (MFU-4-F)	3.24	6.66	2.1	6.0	31
NUM-14a ([Ni(TPT)(NPC)(H_2O)])	3.70	4.44	1.2	3.3	32
[Ca(dtztp)$_{0.5}$]	4.20	4.90	1.2	1.7	33
[Ni(tzba)$_{0.5}$(F)(bpy)]	3.79	5.58	1.5	2.2	34
CAU-10H	2.90	3.90	1.3	2.5	35

[#] all reported conditions are under 298 K and 1 bar, equimolar selectivity.

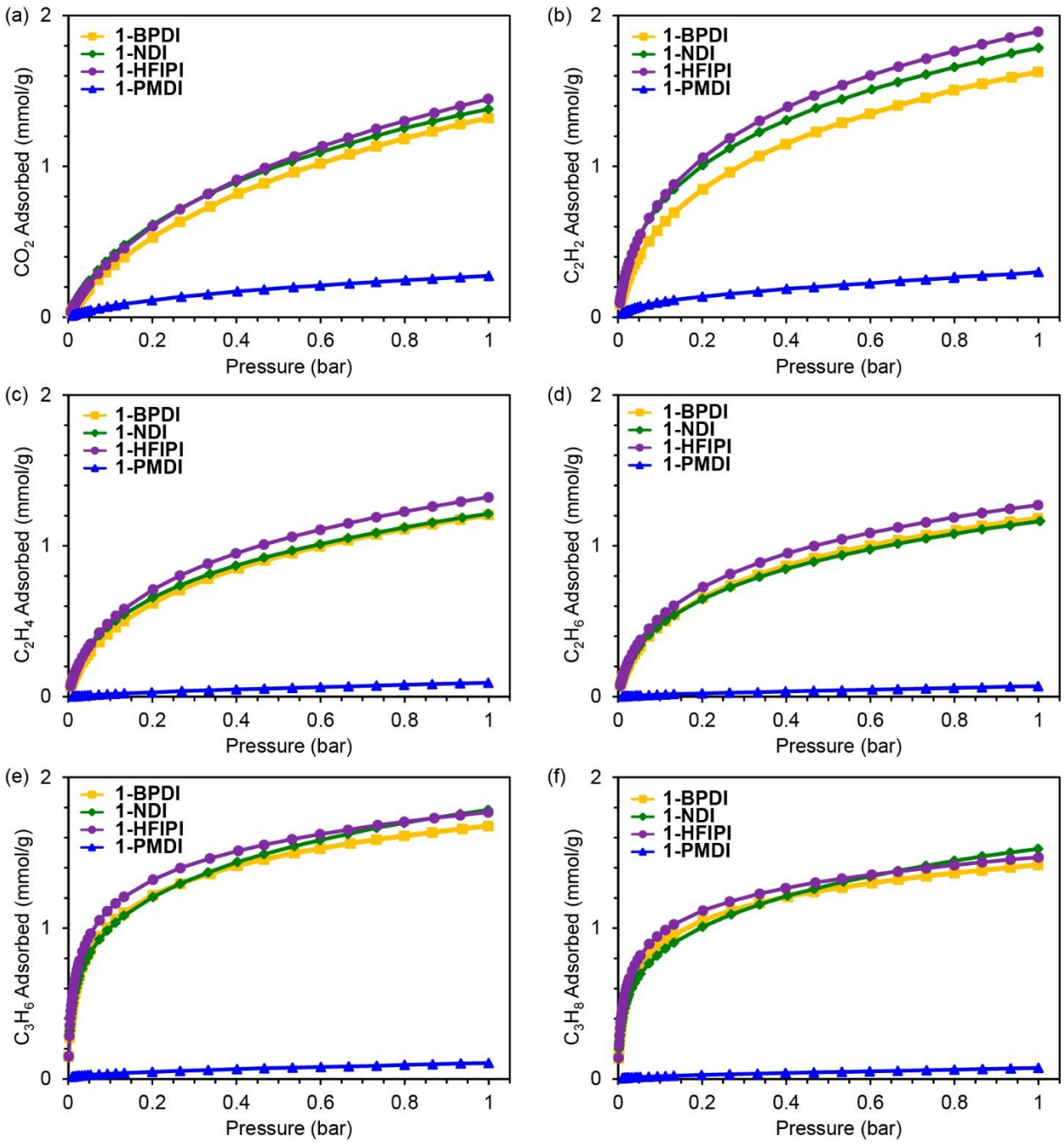

Figure S38. Overlays of the CO_2, C_2H_2, C_2H_4, C_2H_6, C_3H_6, and C_3H_8 adsorption isotherms measured for **1-XDI** materials at 300 K.

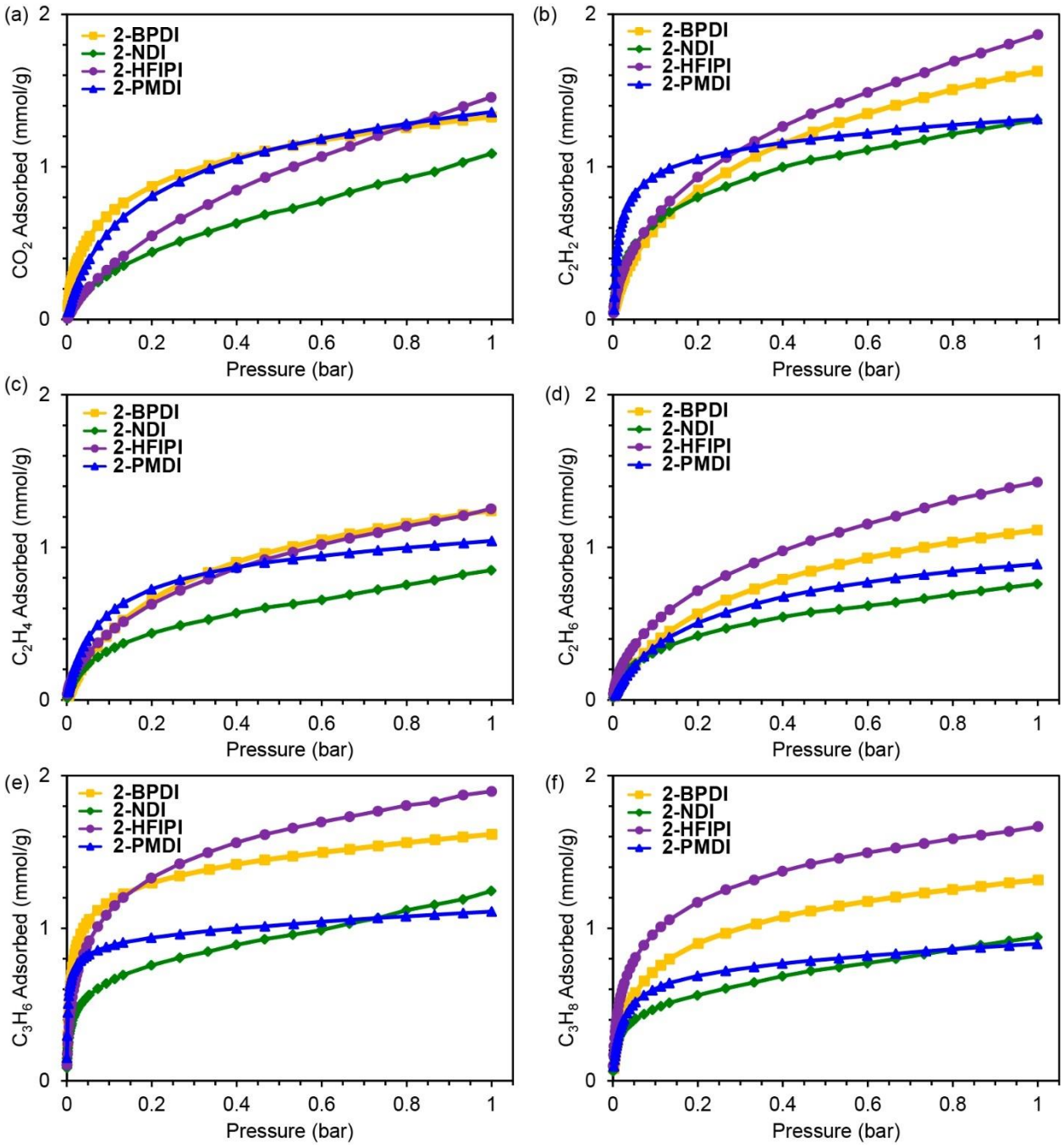

Figure S39. Overlays of the CO_2, C_2H_2, C_2H_4, C_2H_6, C_3H_6, and C_3H_8 adsorption isotherms measured for the **2-XDI** materials at 300 K.

Variable temperature isotherms measured for **1-NDI**, **1-BPDI** and **1-HFIPI** at 300 K, 313 K and 323 K provide zero coverage enthalpy of adsorption ($-\Delta H_{ads}$) values of 33.6 kJ/mol, 29.2 kJ/mol and 35.0 kJ/mol for CO_2, and 46.3 kJ/mol, 46.2 kJ/mol and 43.8 kJ/mol for C_2H_2, respectively (Figure S40-Figure S45). As expected, these values reveal a higher thermodynamic affinity for adsorption of C_2H_2 over CO_2. Moreover, the similarity of the $-\Delta H_{ads}$ values for these materials are also consistent with their similar gas adsorption profiles and IAST selectivity values.

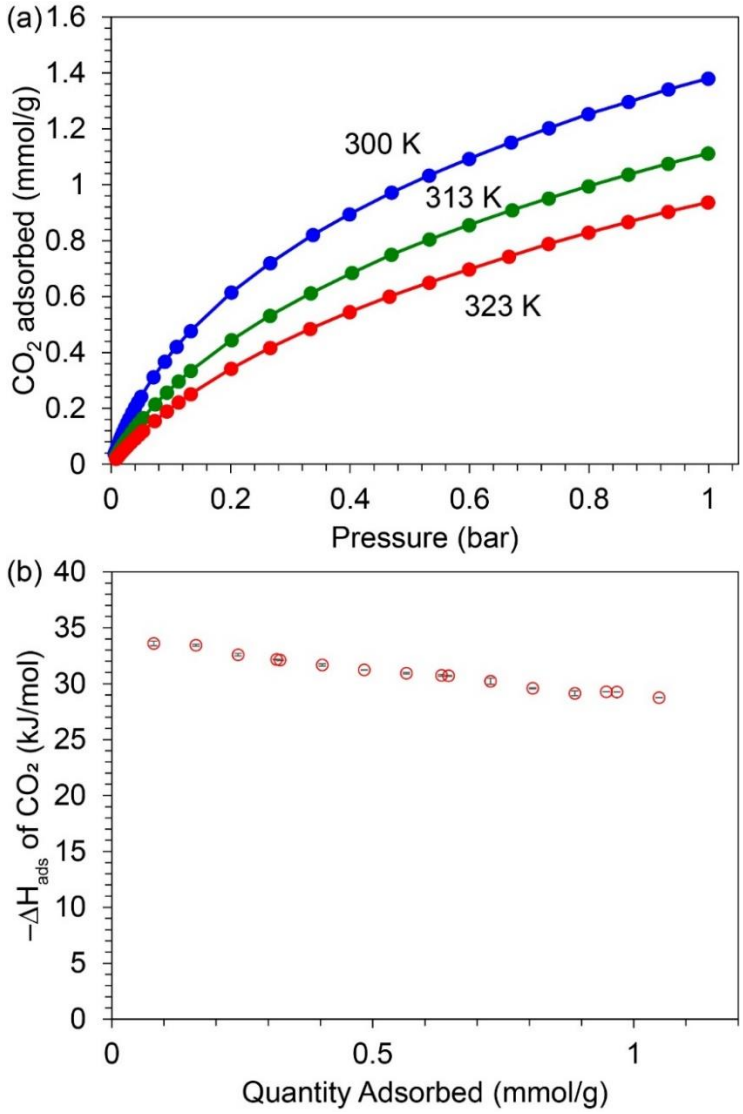

Figure S40. Variable temperature CO_2 adsorption isotherms and isosteric heat of adsorption for **1-NDI.**
(a) Single component CO_2 adsorption isotherms for **1-NDI** measured at 300 K, 313 K and 323 K. (b) The CO_2 adsorption enthalpy as a function of loading calculated from the variable temperature isotherms. The error bars in (b) indicate the uncertainty of the $-\Delta H_{ads}$ value calculated from fitting of the isosteres.

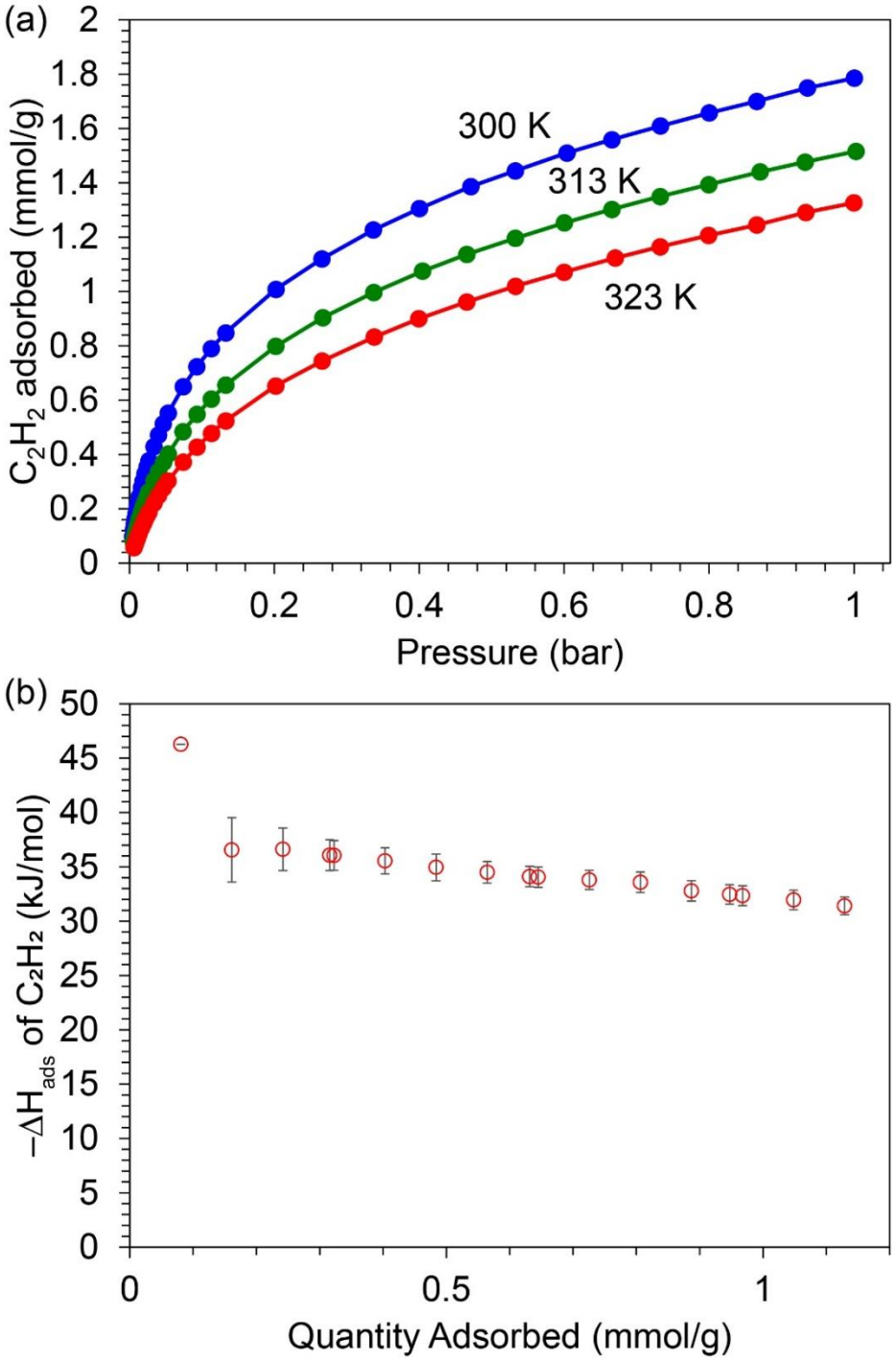

Figure S41. Variable temperature CO_2 adsorption isotherms and isosteric heat of adsorption for **1-NDI**.
a) Single component C_2H_2 adsorption isotherms for **1-NDI** measured at 300 K, 313 K and 323 K. (b) The C_2H_2 adsorption enthalpy as a function of loading calculated from the variable temperature isotherms. The error bars in (b) indicate the uncertainty of the $-\Delta H_{ads}$ value calculated from fitting of the isosteres.

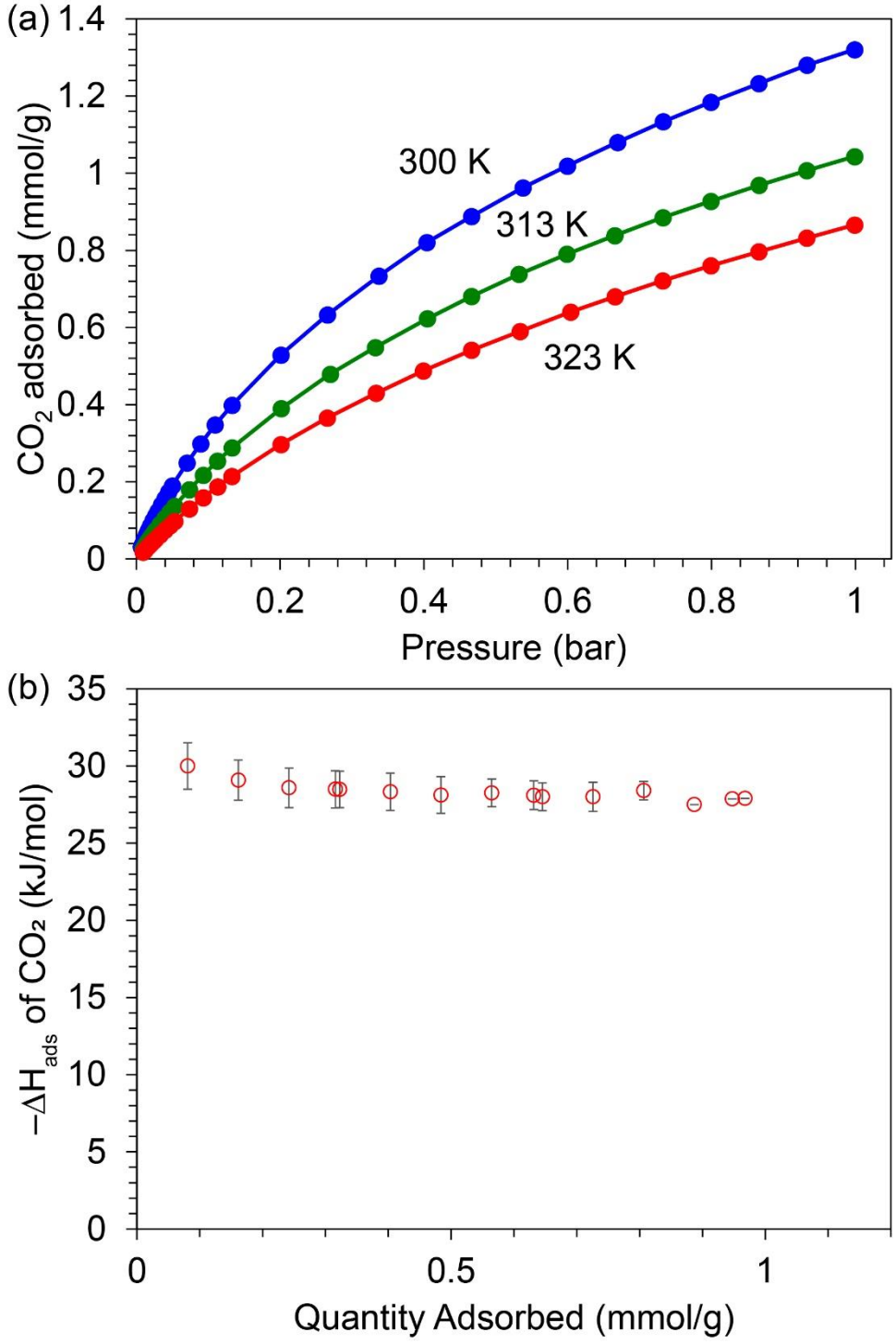

Figure S42. Variable temperature CO_2 adsorption isotherms and isosteric heat of adsorption for **1-BPDI**.
(a) Single component CO_2 adsorption isotherms for **1-BPDI** measured at 300 K, 313 K and 323 K. (b) The CO_2 adsorption enthalpy as a function of loading calculated from the variable temperature isotherms. The error bars in (b) indicate the uncertainty of the $-\Delta H_{ads}$ value calculated from fitting of the isosteres.

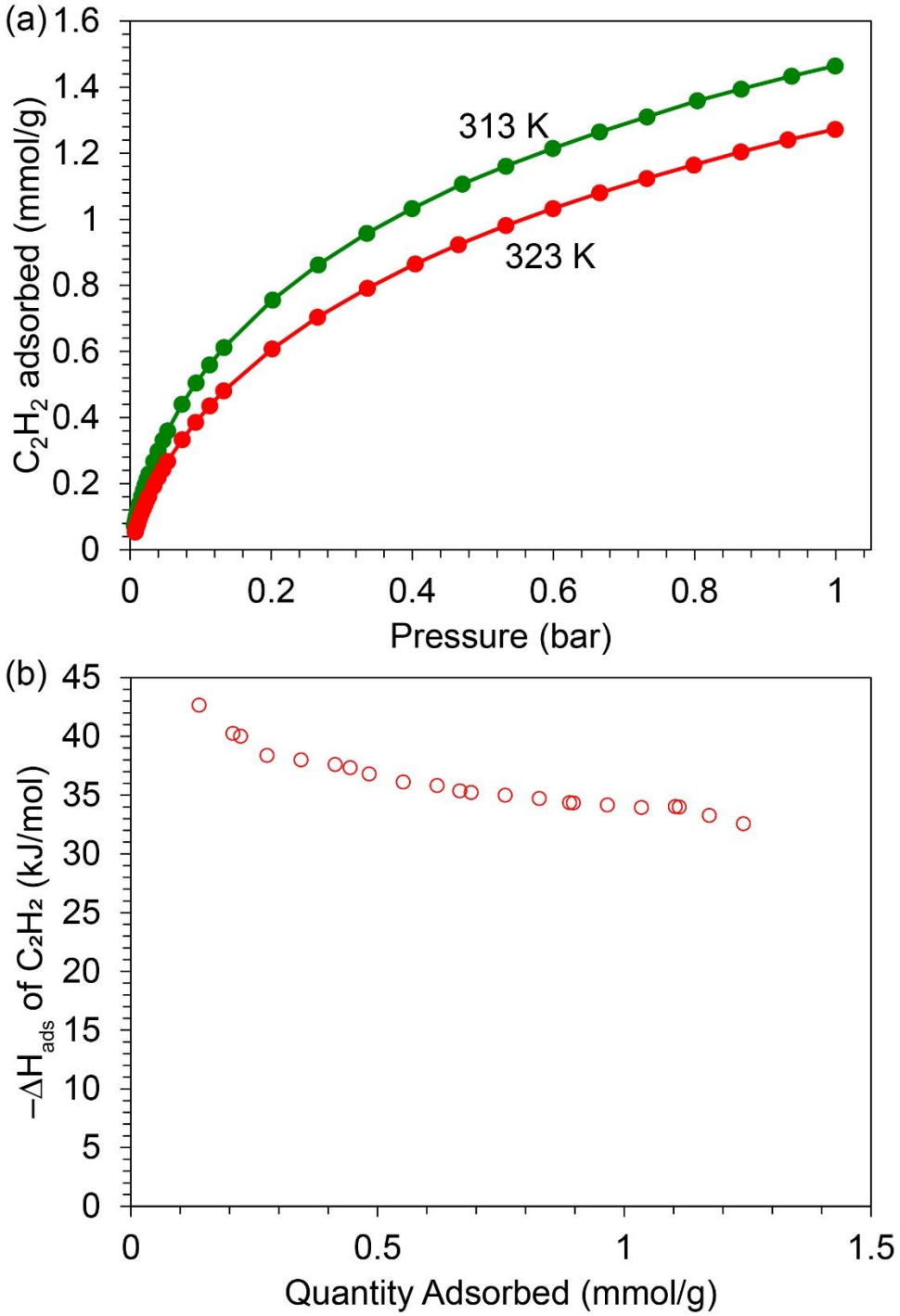

Figure S43. Variable temperature CO_2 adsorption isotherms and isosteric heat of adsorption for **1-BPDI**.
(a) Single component C_2H_2 adsorption isotherms for **1-BPDI** measured at 313 K and 323 K. (b) The C_2H_2 adsorption enthalpy as a function of loading calculated from the variable temperature isotherms.

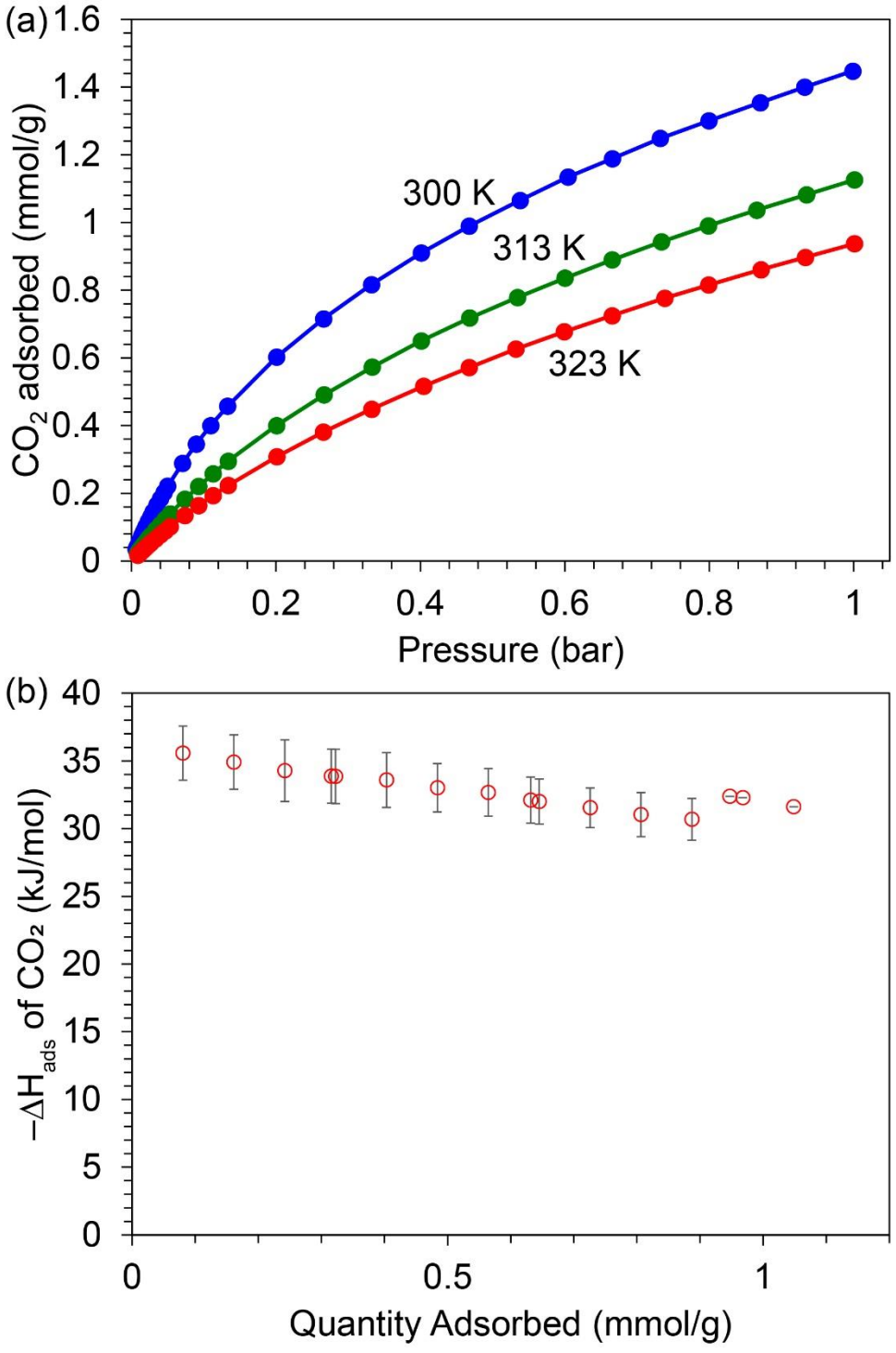

Figure S44. Variable temperature CO_2 adsorption isotherms and isosteric heat of adsorption for **1-HFIPI**.
(a) Single component CO_2 adsorption isotherms for **1-HFIPI** measured at 300 K, 313 K and 323 K. (b) The CO_2 adsorption enthalpy as a function of loading calculated from the variable temperature isotherms. The error bars in (b) indicate the uncertainty of the $-\Delta H_{ads}$ value calculated from fitting of the isosteres.

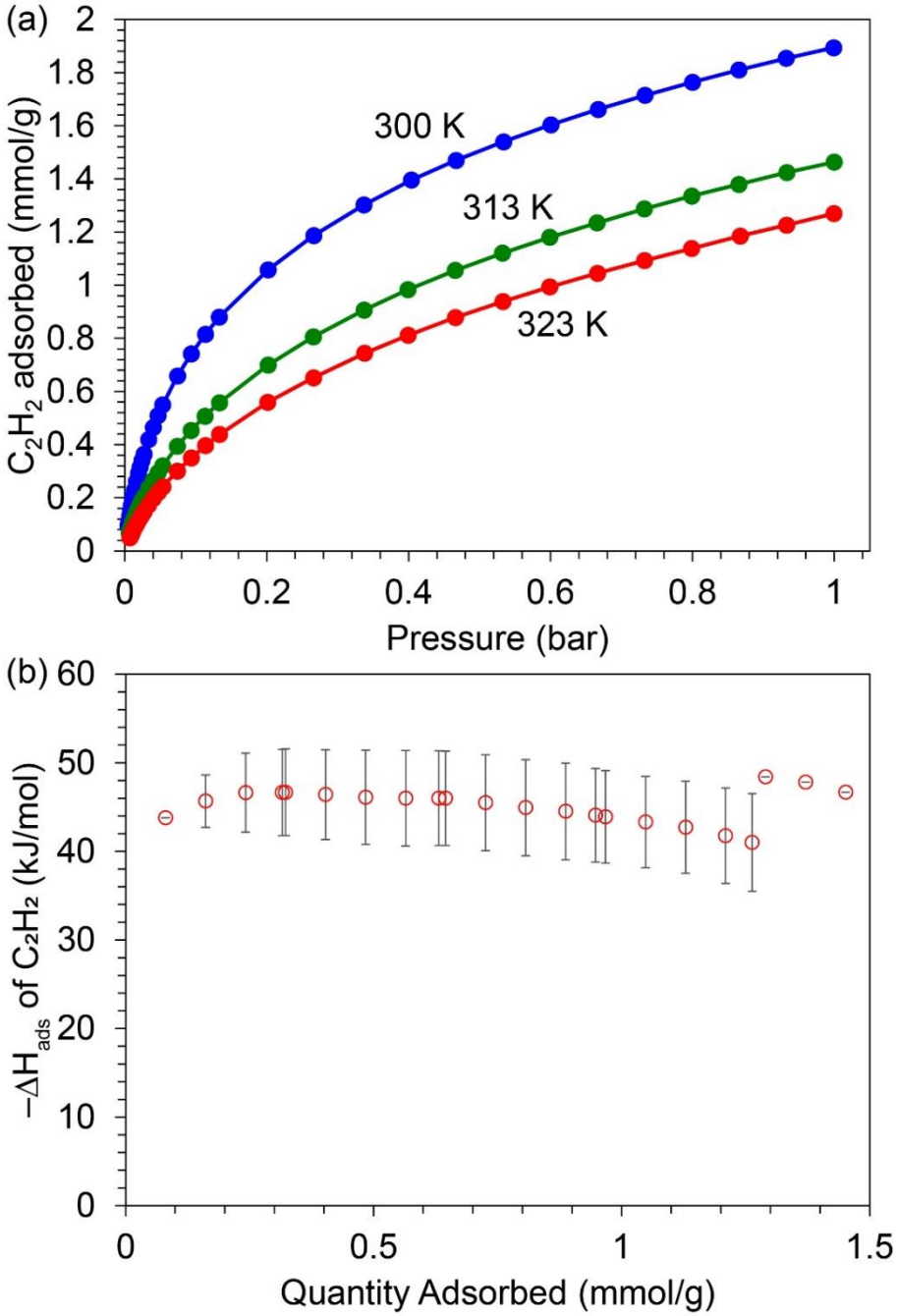

Figure S45. Variable temperature CO_2 adsorption isotherms and isosteric heat of adsorption for **1-HFIPI**.
(a) Single component C_2H_2 adsorption isotherms for **1-HFIPI** measured at 300 K, 313 K and 323 K. (b) The C_2H_2 adsorption enthalpy as a function of loading calculated from the variable temperature isotherms. The error bars in (b) indicate the uncertainty of the $-\Delta H_{ads}$ value calculated from fitting of the isosteres.

References

1 W. Rong-Jia, Z. Hou-Gan, Z. Zhi-Yin, N. Guo-Hong and L. Dan, *CCS Chem.*, 2020, **3**, 2045–2053.

2 X. Li, J. Wang, F. Xue, Y. Wu, H. Xu, T. Yi and Q. Li, *Angew. Chem. Int. Ed.*, 2021, **60**, 2534–2540.

3 H.-G. Zhou, R.-Q. Xia, J. Zheng, D. Yuan, G.-H. Ning and D. Li, *Chem. Sci.*, 2021, **12**, 6280–6286.

4 H.-S. Lu, W.-K. Han, X. Yan, C.-J. Chen, T. Niu and Z.-G. Gu, *Angew. Chem. Int. Ed.*, 2021, **60**, 17881–17886.

5 H. L. Nguyen, F. Gándara, H. Furukawa, T. L. H. Doan, K. E. Cordova and O. M. Yaghi, *J. Am. Chem. Soc.*, 2016, **138**, 4330–4333.

6 S. K. Elsaidi, M. H. Mohamed, J. S. Loring, B. P. McGrail and P. K. Thallapally, *ACS Appl. Mater. Interfaces*, 2016, **8**, 28424–28427.

7 L. Sun, M. Lu, Z. Yang, Z. Yu, X. Su, Y.-Q. Lan and L. Chen, *Angew. Chem. Int. Ed.*, 2022, **61**, e202204326.

8 W.-K. Han, Y. Liu, X. Yan, Y. Jiang, J. Zhang and Z.-G. Gu, *Angew. Chem. Int. Ed.*, 2022, **61**, e202208791.

9 R. Jangir, A. C. Kalita, D. Kaleeswaran, S. K. Gupta and R. Murugavel, *Chem. Eur. J.*, 2018, **24**, 6178–6190.

10 J. Yan, B. Zhang and Z. Wang, *ACS Appl. Mater. Interfaces*, 2018, **10**, 26618–26627.

11 G. Li and Z. Wang, *J. Phys. Chem. C*, 2013, **117**, 24428–24437.

12 G. Li and Z. Wang, *Macromolecules*, 2013, **46**, 3058–3066.

13 E. Rangel Rangel, E. M. Maya, F. Sánchez, J. de Abajo and J. G. de la Campa, *J. Memb. Sci.*, 2013, **447**, 403–412.

14 D. Kołbuk, M. Ciechomska, O. Jeznach and P. Sajkiewicz, *RSC Adv.*, 2022, **12**, 4016–4028.

15 B. R. Reiner, B. M. Foxman and C. R. Wade, *Dalton Trans.*, 2017, **46**, 9472–9480.

16 S. Biswas, M. Grzywa, H. P. Nayek, S. Dehnen, I. Senkovska, S. Kaskel and D. Volkmer, *Dalton Trans.*, 2009, **9226**, 6487–6495.

17 D. Denysenko, M. Grzywa, M. Tonigold, B. Streppel, I. Krkljus, M. Hirscher, E. Mugnaioli, U. Kolb, J. Hanss and D. Volkmer, *Chem. Eur. J.*, 2011, **17**, 1837–1848.

18 P. Schmieder, M. Grzywa, D. Denysenko, M. Hambach and D. Volkmer, *Dalton Trans.*, 2015, **44**, 13060–13070.

19 Q. Liu, N. Hoefer, G. Berkbigler, Z. Cui, T. Liu, A. C. Co, D. W. McComb and C. R. Wade, *Inorg. Chem.*, 2022, **61**, 18710–18718.

20 Z. Chang, R.-B. Lin, Y. Ye, C. Duan and B. Chen, *J. Mater. Chem. A*, 2019, **7**, 25567–25572.

21 Y. Wang, N.-Y. Huang, X.-W. Zhang, H. He, R.-K. Huang, Z.-M. Ye, Y. Li, D.-D. Zhou, P.-Q. Liao, X.-M. Chen and J.-P. Zhang, *Angew. Chem. Int. Ed.*, 2019, **58**, 7692–7696.

22 Y. Xie, Y. Shi, H. Cui, R.-B. Lin and B. Chen, *Small Struct.*, 2022, **3**, 2100125.

23 D.-L. Chen, H. Shang, W. Zhu and R. Krishna, *Chem. Eng. Sci.*, 2014, **117**, 407–415.

24 J. E. Bachman, M. T. Kapelewski, D. A. Reed, M. I. Gonzalez and J. R. Long, *J. Am. Chem. Soc.*, 2017, **139**, 15363–15370.

25 B. Liang, X. Zhang, Y. Xie, R.-B. Lin, R. Krishna, H. Cui, Z. Li, Y. Shi, H. Wu, W. Zhou and B. Chen, *J. Am. Chem. Soc.*, 2020, **142**, 17795–17801.
26 Y. Xie, Y. Shi, E. M. Cedeño Morales, A. El Karch, B. Wang, H. Arman, K. Tan and B. Chen, *J. Am. Chem. Soc.*, 2023, **145**, 2386–2394.
27 L. Zhang, K. Jiang, L. Yang, L. Li, E. Hu, L. Yang, K. Shao, H. Xing, Y. Cui, Y. Yang, B. Li, B. Chen and G. Qian, *Angew. Chem. Int. Ed.*, 2021, **60**, 15995–16002.
28 Z. Niu, X. Cui, T. Pham, G. Verma, P. C. Lan, C. Shan, H. Xing, K. A. Forrest, S. Suepaul, B. Space, A. Nafady, A. M. Al-Enizi and S. Ma, *Angew. Chem. Int. Ed.*, 2021, **60**, 5283–5288.
29 W. Gong, H. Cui, Y. Xie, Y. Li, X. Tang, Y. Liu, Y. Cui and B. Chen, *J. Am. Chem. Soc.*, 2021, **143**, 14869–14876.
30 G.-R. Si, W. Wu, T. He, Z.-C. Xu, K. Wang and J.-R. Li, *ACS Mater. Lett.*, 2022, **4**, 1032–1036.
31 Q. Liu, S. G. Cho, J. Hilliard, T.-Y. Wang, S.-C. Chien, L.-C. Lin, A. C. Co and C. R. Wade, *Angew. Chem. Int. Ed.*, 2023, **62**, e202218854.
32 Q. Zhang, G.-N. Han, X. Lian, S.-Q. Yang and T.-L. Hu, *Molecules*, 2022, **27**, 5929–5939.
33 G.-D. Wang, Y.-Z. Li, W.-F. Zhang, L. Hou, Y.-Y. Wang and Z. Zhu, *ACS Appl. Mater. Interfaces*, 2021, **13**, 58862–58870.
34 G.-D. Wang, H.-H. Wang, W.-J. Shi, L. Hou, Y.-Y. Wang and Z. Zhu, *J. Mater. Chem. A*, 2021, **9**, 24495–24502.
35 Y. Ye, S. Xian, H. Cui, K. Tan, L. Gong, B. Liang, T. Pham, H. Pandey, R. Krishna, P. C. Lan, K. A. Forrest, B. Space, T. Thonhauser, J. Li and S. Ma, *J. Am. Chem. Soc.*, 2022, **144**, 1681–1689.